Potential Vorticity Diagnostics of Cyclogenesis

CHRISTOPHER A. DAVIS* AND KERRY A. EMANUEL

Center for Meteorology and Physical Oceanography, Massachusetts Institute of Technology, Cambridge, Massachusetts

(Manuscript received 1 October 1990, in final form 25 February 1991)

ABSTRACT

The assumption of dynamically balanced flow allows one to completely encase the dynamics of extratropical cyclones in a potential vorticity (PV) framework. This approach offers a conceptually simple interpretation of dynamics because PV is a conserved quantity (in the absence of heating and friction) from which the flow itself can be deduced (the property of invertibility). The conservation law allows one to identify developments significantly influenced by heating and friction, and the invertibility property can be used to quantitatively measure such effects. We develop a diagnostic system based on the relative smallness of the irrotational part of the horizontal wind, which allows us to calculate the balanced flow given the three-dimensional distribution of Ertel's PV. The close agreement between the observed and balanced flows, even for intense cyclones, illustrates the practical utility of the PV approach. Furthermore, we present a technique for determining the flow associated with individual perturbations of PV.

Insight gained from these diagnostics is demonstrated by examining a particular case of cyclogenesis. In the early stages of growth, the low-level perturbation winds are mostly associated with variations of potential temperature along the lower boundary and act to propagate the system as a surface Rossby wave. Amplification of this wave occurs through advection, first by the winds associated with a low-level PV feature, then later by the low-level circulation signature of an amplifying upper-level wavelike PV anomaly. In turn, development of the upper-level perturbation appears strongly influenced by the presence of the low-level anomalies. The low-level PV anomaly seems to result from the condensation of water vapor rather than from advection. This feature grows rapidly, eventually contributing about 40% of the cyclonic circulation in the mature storm. We do not identify any significant PV anomalies arising from advection on a systematic tropospheric PV gradient, implying that the integrated effect of β is dominated by the gradient of PV at the tropopause. Viewing the upper-level wave as a perturbation of potential temperature on the tropopause (a surface of constant PV), part of this development is conceptualized as interacting upper and lower boundary Rossby waves, as in the Eady model.

1. Introduction

a. Remaining problems

Observational analysis, interpretation, and forecasting of midlatitude cyclone and anticyclone behavior have constituted an important branch of meteorological research for many decades. The extraordinary attention given to studying these extratropical systems likely stems from their intimate connection with weather and weather prediction. Our ability to forecast cyclone and anticyclone behavior has increased to the point where accurate forecasts of two days and longer are routine. However, a proper integration of the equations of motion is not synonymous with a conceptual grasp of the phenomena being predicted. Indeed, the emphasis on forecasting may have contributed to an unhealthy separation between observational and theoretical work on cyclone dynamics. Observations and theory have yet to be reconciled on some important topics and there has not been enough work to separate the underlying physics of cyclone development from unsystematic details of individual cases. These are necessary if a simple conceptual picture of cyclogenesis is to emerge. A conceptual understanding is not only useful for reconciling theory with observation, but it is also valuable for delineating measurements necessary for accurately integrating forecast models.

A well-accepted theoretical explanation for cyclogenesis is baroclinic instability, that is, the quasi-exponential growth of an initially small amplitude disturbance on an unstable basic state (Charney 1947; Eady 1949). However, as pointed out by Petterssen et al. (1955) and Sanders (1986, 1988), large amplitude disturbances in the upper troposphere are often present before development at the surface commences. This observation has been part of the motivation for examining the initial value problem of baroclinic growth (Farrell 1984, 1989) in which the structure of the initial perturbation, rather than the stability characteristics of the basic state, determines whether development will

---

* Current affiliation: National Center for Atmospheric Research, MMM division, Boulder, Colorado 80307.

Corresponding author address: Dr. Christopher A. Davis, NCAR, P.O. Box 3000, Boulder, CO 80307.

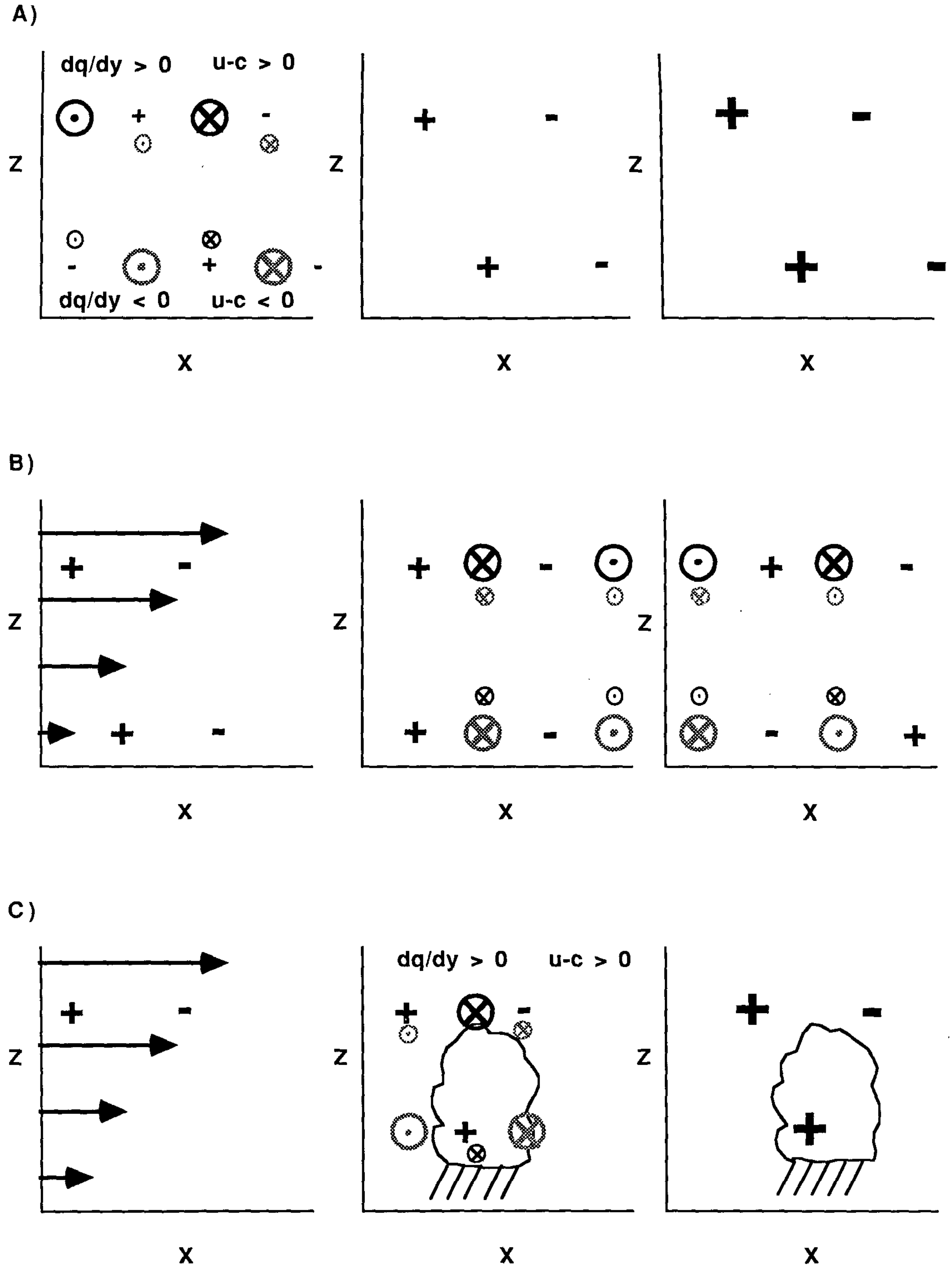

FIG. 1. Schematic illustration of three types of baroclinic development based on fundamentally different PV behavior. Panels (a), (b), and (c) represent mutual interaction, superposition, and growth induced by diabatic processes, respectively. PV anomalies are indicated by "+" and "−" signs (size is proportional to strength); their associated meridional winds are represented by circles. There are two rows of PV anomalies; these represent upper and lower tropospheric disturbances in our case. Circles containing an "×" denote wind into the page (southerly); circles with a dot indicate wind out of the page (northerly). Circle size qualitatively represents strength of flow. Large circles denote winds at the same level as their corresponding PV anomalies; small circles represent the winds associated with PV anomalies at the other level. Circles in darker print denote winds from upper PV anomalies; lighter circles depict winds from lower-level PV anomalies. Large arrows at left in (b) and (c) represent the vertical shear of the basic-state zonal current. This shear also is present in example (a), but vectors were removed for clarity.

occur. Because the growing, the decaying normal modes do not generally form a complete set; a continuous spectrum of neutral modes must be included to represent an arbitrary perturbation. Therefore, the structure of the initial value problem solution evolves with time, as does its amplitude. The time dependence is initially algebraic, in contrast to the exponential behavior of normal modes.

The distinction between modal and nonmodal growth per se is perhaps most appropriate for theoretical rather than observational investigation. Because observed, instantaneous atmospheric states are not steady, one cannot determine a unique set of normal modes. In addition, even normal modes on idealized basic states will eventually enter a nonlinear regime when their structure evolves (Simmons and Hoskins 1978). However, a question amenable to observational investigation is whether structural transience is *necessary* for growth. Even when a large amplitude upper-tropospheric disturbance is present when low-level development begins, it has not been demonstrated quantitatively whether the subsequent structural evolution that occurs is essential for further intensification.

Another poorly understood problem is the feedback of clouds and precipitation onto the dynamics of cyclones via the release of latent heat. A multitude of investigations have examined this effect on observed cyclones (Manabe 1956; Eliassen and Kleinschmidt 1957; Danard 1964; Tracton 1974; Gyakum 1983; Kuo and Reed 1988; Emanuel 1988; Kuo et al. 1990a), and opinions vary as to its significance. Although Kleinschmidt believed that moisture was essential for development, most investigators have cast latent heat release in the role of accelerating growth destined to occur even in its absence. The nonlinearities imposed by the presence of water vapor complicate attempts to isolate its significance using observations. At any instant, one may deduce the tendencies due to condensation, if one knows the distribution of latent heating. Yet, the instantaneous state has itself been irreversibly altered by latent heat release. A deeper understanding of the effect of moisture requires us to integrate the changes from condensation in time. An adequate conceptual picture must describe how the perturbations created by condensation interact with the rest of the fluid.

Many investigations concern the influence of moisture on the mature cyclone's intensity. However, of considerable importance is how the cyclone structure and propagation are altered by the presence of moisture during all phases of development. This issue was partly addressed theoretically by Emanuel et al. (1987) who proposed, based on observations, that condensation takes place under slantwise neutral conditions. The resulting structure of two-dimensional, baroclinic waves with this constraint exhibited an intense updraft of very small horizontal scale, but a nearly unchanged descent region. The characteristic strong, sloping updraft has been noted in numerical simulations of intense cyclones (Uccellini et al. 1987; Kuo et al. 1990b) and in observations (Sanders and Bosart 1985). The full three-dimensional picture of the influence of condensation on the life cycle of baroclinic waves is still incomplete, however.

b. Potential vorticity approach

An apparent need exists for a better diagnostic framework in which to study cyclogenesis that allows quantitative analysis of data while facilitating a subjective understanding of the physics involved. We desire a formalism that provides a convenient basis for the intercomparison of observation, theory, and modeling results. Perhaps the most fundamental approach is to diagnose developments in terms of conserved quantities that carry the relevant dynamical information of the system. Absolute vorticity is such a quantity in a nondivergent, barotropic fluid because it is conserved and may be inverted to recover the exact flow field. Thus, with conservation and invertibility, all the dynamics are succinctly embodied in a single scalar quantity and in certain boundary conditions.

For a fully baroclinic, compressible flow, absolute vorticity in a barotropic fluid generalizes to Ertel's potential vorticity (EPV)[1]:

$$q = \frac{1}{\rho} \boldsymbol{\eta} \cdot \nabla \theta, \tag{1.1}$$

which is conserved following three-dimensional, adiabatic, inviscid motion (Rossby 1940; Ertel 1942). Here $\boldsymbol{\eta}$ is the absolute vorticity vector, θ the potential temperature, and ρ the density. Specification of an independent relation between the wind and temperature fields allows one to define a boundary value problem from which the "balanced" flow is recovered given the distribution of q (Hoskins et al. 1985; hereafter, HMR). The statement of invertibility, specified by this boundary value problem, depends on the precise balance assumption used. In a nondivergent, barotropic fluid, the balanced flow and actual flow are identical. In the atmosphere, the balanced flow is only an approximation to the total flow, the accuracy of which depends on the validity of scaling assumptions used to define the invertibility problem.

One commonly used equation system that approximates EPV conservation is quasi geostrophy (QG). The quasi-geostrophic pseudopotential vorticity (PPV, Charney and Stern 1962) is defined

$$q_p = \nabla^2 \psi + f_0 + \beta(y - y_0) + \frac{f_0^2}{\bar{\rho}} \left(\frac{\bar{\rho}}{N^2} \psi_z \right)_z, \tag{1.2}$$

---

[1] The abbreviation PV will refer to potential vorticity in general without reference to a specific form.

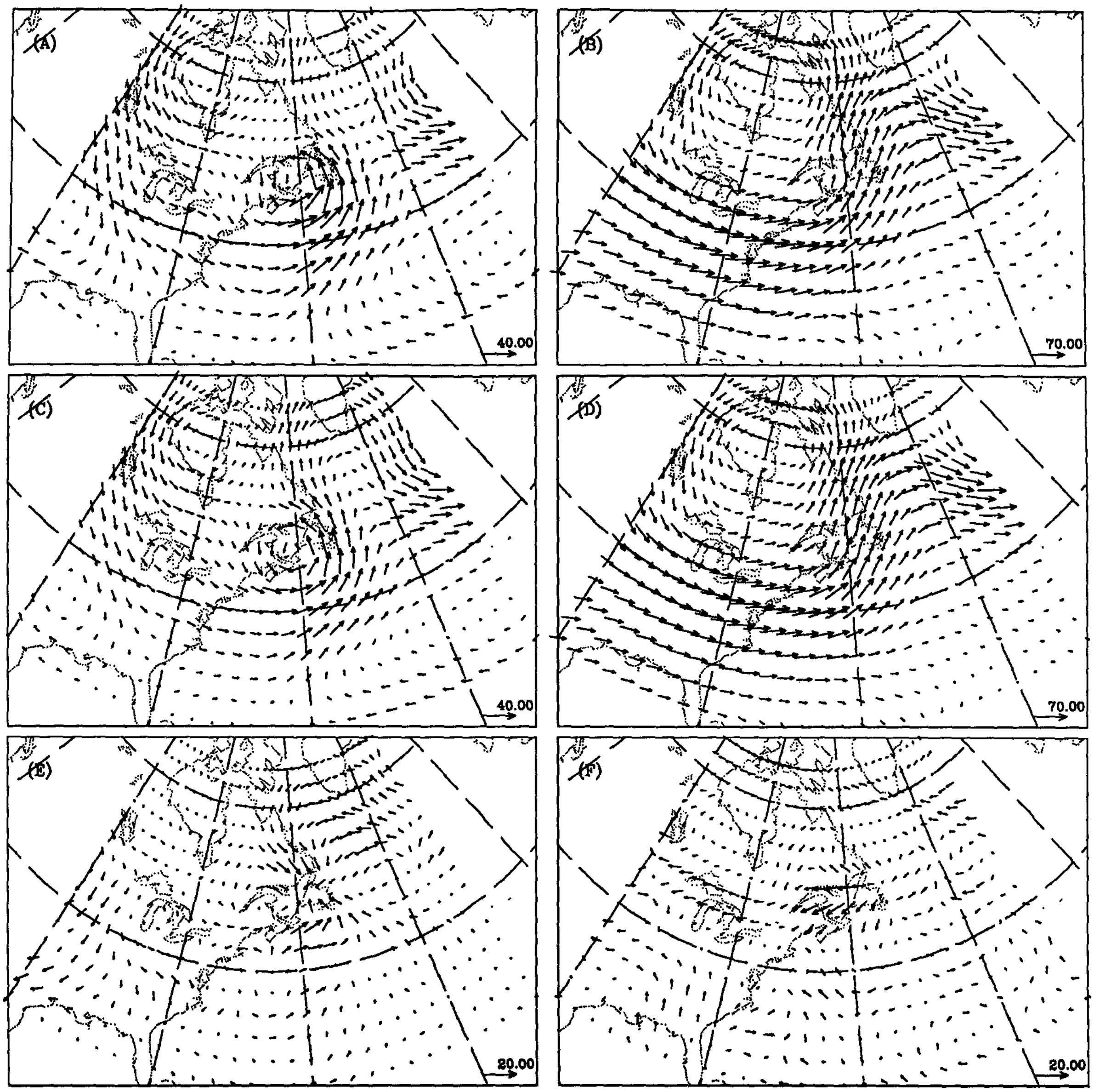

FIG. 4. (a), (c), (e), and (g) show balanced 1000-mb heights for 0000 UTC 4 February, 1200 UTC 4 February, 0000 UTC 5 February, and 1200 UTC 5 February 1988, respectively. Panels (b), (d), (f), and (h) are 500-mb balanced heights for the same times. Dashed contours denote negative 1000-mb heights. Heavy dashed lines are parallel to the mean 1000–400-mb shear and show the orientation of the cross sections presented in Fig. 14.

where ψ is the geostrophic streamfunction, $\bar{\rho}$ and N_2 are functions of z alone, and we have employed a beta-plane geometry ($\beta = df/dy|_{y=y_0}$). The QG system of equations reduces to conservation of q_p following the geostrophic wind, a valid statement provided the Rossby number is $\ll O(1)$ and heating and friction are absent. For departures of PPV from a zonal or time average, (1.2) becomes essentially a Poisson equation in three dimensions, hence, one can readily deduce the geostrophic flow associated with individual anomalies of PPV. In particular, an isolated maximum of q_p in the Northern Hemisphere will be associated with a minimum in ψ, and a maximum in vorticity and static stability (and the opposite for a q_p minimum). As Kleinschmidt and HMR note, these general properties also hold for inversions of EPV using higher-order balance approximations. In addition, perturbations of potential temperature at the lower boundary can be thought of as PV anomalies (Bretherton 1966), with locally warm air associated with cyclonic vorticity and cold anomalies related to anticyclonic vorticity.

The linear form of (1.2) implies that any state can be decomposed into a set of individual anomalies of PPV, whose associated circulations sum to the total flow. For small Rossby numbers, nonconservation will occur from either diabatic heating or frictional processes, and the resulting PPV anomalies can be inverted to deduce the part of the flow directly associated with that process. The winds associated with these anomalies are, of course, free to interact with other nearby PPV features.

As suggested by HMR, diagnostics based on potential vorticity are valuable for testing theoretical models of development. Figure 1 is a schematic illustrating three possible mechanisms of cyclogenesis distinguished by their potential vorticity evolution. These can be briefly summarized as (a) mutual reinforcement between phase-locked Rossby waves at different altitudes (akin to the description of baroclinic instability in HMR). The perturbation structure in this example remains fixed during development and the PV anomalies grow; (b) simple superposition of PV anomalies. With no mean PV gradient, the anomalies remain fixed in amplitude, but the structure evolves, allowing the circulations to add (middle figure) and later cancel (right figure) as the shear flow (arrows at left) advects the upper wave downshear. While potential enstrophy is unchanged in this process, the perturbation energy increases at the expense of the basic-state shear flow; (c) development induced by generation of PV anomalies through condensation, similar to Kleinschmidt's idea (Eliassen and Kleinschmidt 1957). Some circulation increase at low levels occurs from the generation of low-level PV alone. However, there can also be baroclinic interaction between the lower and upper anomalies (Montgomery and Farrell 1991). A fourth scenario, not depicted, occurs when a PV anomaly enters a region of enhanced or reduced Rossby penetration depth and the strength of the circulation at a distance from the anomaly is altered.

Compare this perspective with the classification scheme of Petterssen and Smebye (1971, hereafter PS) who consider two types of cyclogenesis, frontal waves (type A) and developments with a strong upper-level precursors (type B). Although there are several ambiguities in their categorization method, especially concerning the importance of surface baroclinicity, perhaps the biggest drawback is the qualitative nature of the distinction between type A and type B. In addition, there may be considerable geographical bias in these descriptions and they are limited to describing surface cyclogenesis. The PV approach allows one to pick out the underlying dynamics and describe developments at any atmospheric level or any geographical location in terms of a small number of fundamentally different scenarios.

QG diagnostics, emphasizing PPV distributions, are a valuable tool for diagnosing weak developments. However, there are few studies that apply both the invertibility and conservation properties of potential vorticity (in any form) to observations (Robinson 1987). It is logical to focus diagnostics on Ertel's PV because its conservation does not depend on scaling assumptions.[2] An exact invertibility statement for EPV does not exist. However, we will develop an approximate diagnostic system based on the smallness of the irrotational wind compared to the nondivergent wind. A prognostic system based on this scaling does exist,

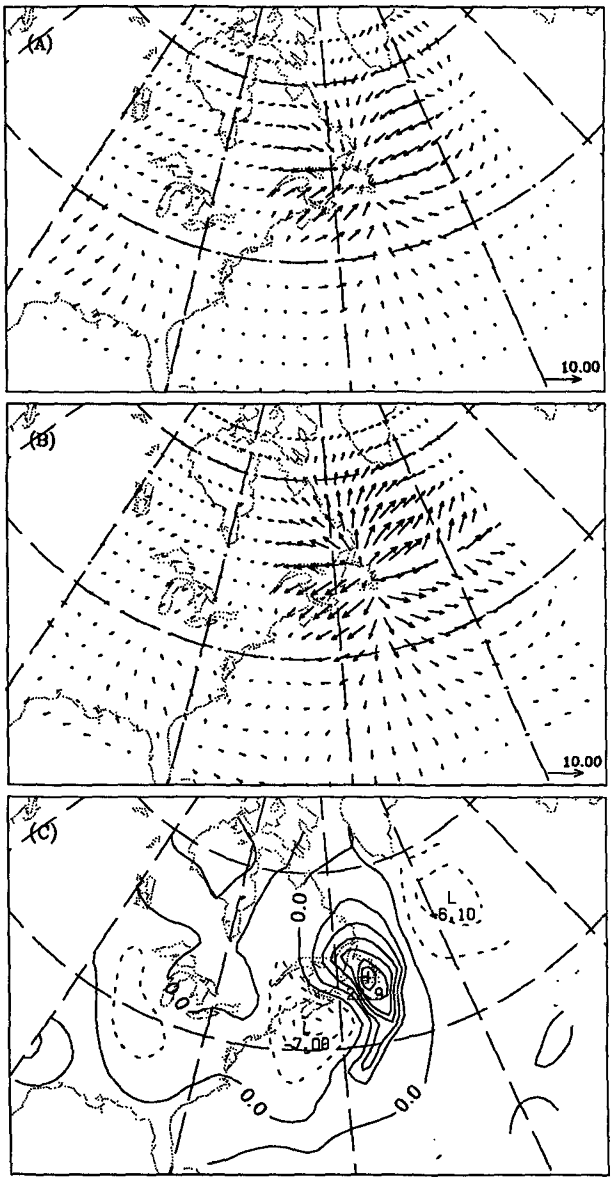

FIG. 3. (a) Irrotational winds at 850 mb, (b) irrotational winds at 400 mb, (c) vertical velocity ($w = dz/dt$) at 600 mb [dashed lines (negative values) contoured at 2 cm s^{-1} intervals, solid lines at 3 cm s^{-1} intervals]. All quantities are derived from the prognostic balance equations presented in appendix B. Note the difference in vector length scale from Figs. 2e and 2f.

---

[2] We assume that the transport of PV is not dominated by eddies unresolved by observations.

known as the "balance equations" (Charney 1962). Although we are not aware of a formal conservation relation for an approximation to EPV in this system, the accuracy of the Charney balance equation (Charney 1955; Gent and McWilliams 1983) motivates its adoption as the anchor of our diagnostic system.

The remainder of the paper is organized into two basic parts. First, we outline the derivation of a diagnostic system based on Ertel's PV (section 2). In section 3, we present the application of these diagnostics to a particular case of development. We discuss the relative roles of mutual amplification of Rossby waves, superposition, and condensation of water vapor. The final sections of this paper include a discussion of the development in terms of existing theoretical models of baroclinic growth. We also suggest further calculations to be done for this case and outline other avenues of research.

2. The diagnostic system

Here we develop a diagnostic system from which the wind and temperature perturbations associated with a given distribution of perturbation EPV may be obtained. First, we discuss how to obtain the balanced flow from the total EPV. We then demonstrate that the nondivergent winds of the observed flow are nearly identical to balanced winds, implying that we can account for the full intensity of circulation systems by focusing solely on the EPV. The specific definitions of mean and perturbation are then discussed, and finally, a set of equations is derived, which uniquely relates EPV and flow perturbations.

a. The equations

The balance condition we shall employ was derived by Charney (1955), and is very accurate in flows with large curvature because it is quite similar to gradient wind balance. The Charney balance equation is obtained by first taking the horizontal divergence of the horizontal momentum equations and decomposing the wind field into a nondivergent and an irrotational part. Following Haltiner and Williams (1980), we then define two Rossby numbers, $R_\psi = V_\psi/f_0L$ and $R_\chi = V_\chi/f_0L$. We then retain $O(R_\psi)$ terms but neglect terms $O(R_\chi)$ and higher in accordance with our balance assumption. The resulting (dimensional) equation may be written in spherical coordinates (λ, ϕ, a)

$$\nabla^2\Phi = \nabla\cdot(f\nabla\Psi) + \frac{2}{a^4\cos^2\phi}\frac{\partial(\partial\Psi/\partial\lambda, \partial\Psi/\partial\phi)}{\partial(\lambda, \phi)} \tag{2.1}$$

with Φ the geopotential, Ψ the nondivergent streamfunction ($\mathbf{v}_\psi = \mathbf{k}\times\nabla\Psi$), λ is longitude, ϕ is latitude, and a is the earth's radius. Relation (2.1) reduces to geostrophic balance if f is constant and the Jacobian term is neglected.

We need one more diagnostic equation relating Ψ to Φ in order to close the system. This is obtained from an approximate definition of EPV:

$$q = -\frac{g\kappa\pi}{p}\left(\eta\frac{\partial\theta}{\partial\pi} - \frac{1}{a\cos\phi}\frac{\partial v}{\partial\pi}\frac{\partial\theta}{\partial\lambda} + \frac{1}{a}\frac{\partial u}{\partial\pi}\frac{\partial\theta}{\partial\phi}\right), \tag{2.2}$$

where $\kappa = R_d/C_p$, p is the pressure, π is the Exner function $[C_p(p/p_0)^\kappa]$ and serves as our vertical coordinate, η is the vertical component of absolute vorticity and the hydrostatic approximation has been made. We perform a similar scaling of (2.2) as was used to obtain (2.1), yielding a relation between the potential vorticity, Ψ and Φ,

$$q = \frac{g\kappa\pi}{p}\left[(f+\nabla^2\Psi)\frac{\partial^2\Phi}{\partial\pi^2} - \frac{1}{a^2\cos^2\phi}\frac{\partial^2\Psi}{\partial\lambda\partial\pi}\frac{\partial^2\Phi}{\partial\lambda\partial\pi} - \frac{1}{a^2}\frac{\partial^2\Psi}{\partial\phi\partial\pi}\frac{\partial^2\Phi}{\partial\phi\partial\pi}\right]. \tag{2.3}$$

The approximation used here replaces the vertical derivative of the total wind by the vertical derivative of the nondivergent wind. Equations (2.1) and (2.3) form a complete system for the unknowns Φ and Ψ, given q.

For boundary conditions, we prescribe Ψ and Φ on the lateral boundaries and specify their vertical derivatives on the horizontal boundaries. The observed geopotential serves as Φ on the lateral edges and $\partial\Phi/\partial\pi = -\theta$ is applied at the top and bottom. We require the gradient of Ψ along the edge to match the normal wind component

$$\frac{\partial\Psi}{\partial s} = -\mathbf{v}\cdot\mathbf{n} + \frac{\oint \mathbf{v}\cdot\mathbf{n}\,dl}{\oint dl}, \tag{2.4}$$

where $\mathbf{n}$ is the outward normal and s is parallel to the edge (counterclockwise). The last term in (2.4) subtracts any net divergence in the domain and forces the integral of $\partial\Psi/\partial s$ around the edge to vanish. The arbitrary constant of integration is supplied by specifying $\Psi = \Phi$ at one point on the boundary. The condition for Ψ on the horizontal boundaries is $\partial\Psi/\partial\pi = -\theta$, applied at both the top and bottom. This is justified because the term involving the vertical derivative of Ψ in (2.3) is already $O(R_\psi)$. Because a correction to this condition that accounts for nonlinear balance would also be $O(R_\psi)$, it would enter (2.3) as an $O(R_\psi^2)$ term. The solutions we obtain are, in fact, fairly insensitive to this choice of boundary condition.

The method of solution, a rather complicated application of successive overrelaxation (SOR), appears in appendix A. The complexity of the equations, combined with inherent observational inaccuracies present

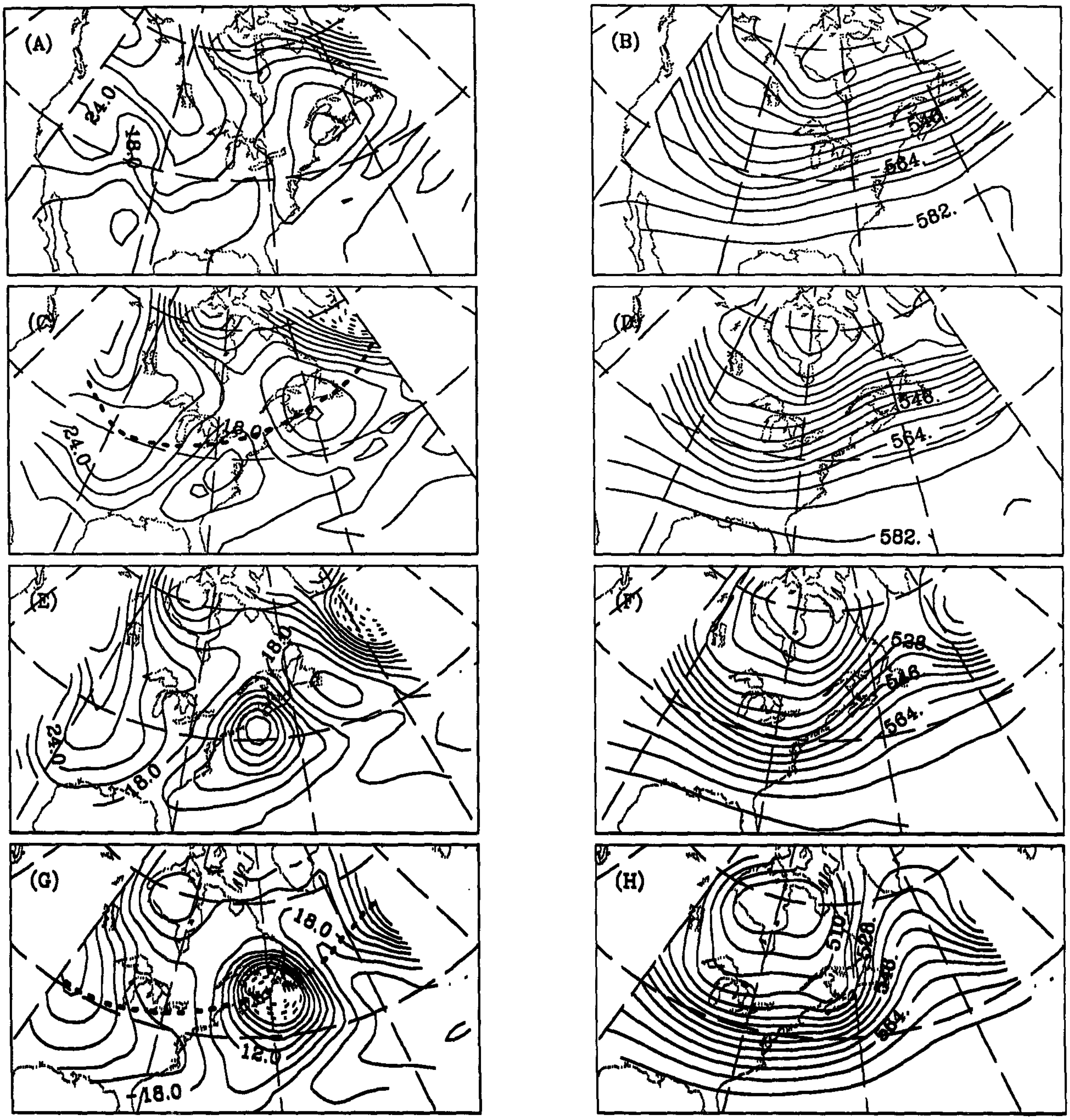

FIG. 4. (a), (c), (e), and (g) show balanced 1000-mb heights for 0000 UTC 4 February, 1200 UTC 4 February, 0000 UTC 5 February, and 1200 UTC 5 February 1988, respectively. Panels (b), (d), (f), and (h) are 500-mb balanced heights for the same times. Dashed contours denote negative 1000-mb heights. Heavy dashed lines are parallel to the mean 1000-mb to 400-mb shear and show the orientation of the cross sections presented in Fig. 14.

in the potential vorticity itself, made an iterative technique the only practical solution method. As long as the EPV was everywhere positive, our technique consistently converged. Tests with different initial guesses showed that the solution obtained was apparently unique, or at least other existing solutions were unreachable.

b. An example

We now show that the "balanced flow" obtained by solving the finite-difference versions of (2.1) and (2.3) accurately reflects the observed winds, with nearly all the differences attributable to divergence. The particular example is from a case of cyclogenesis (to be discussed in detail in section 3) that occurred over eastern North America on 4 and 5 February 1988. The data are taken from the final global analyses of the National Meteorological Center (NMC) (Trenberth and Olsen 1988), a product of the Global Data Analysis System (GDAS) on a 2.5° × 2.5° latitude–longitude grid. The mandatory level[3] fields of wind, temperature, and geopotential height are used to compute EPV on pressure surfaces according to the centered finite-difference analogue of (2.2). The EPV is obtained at mandatory levels ranging from 850 to 150 mb; the mean potential temperature between 1000 and 850 mb (θ_B) specifies our lower boundary condition.[4] The upper boundary value of θ (near 125 mb) is obtained by integrating the static stability upward from θ at the lower boundary (near 925 mb).[5] The winds used to calculate EPV are the total analyzed horizontal winds.

Figure 2 presents winds at 850 and 400 mb for 1200 UTC 5 February 1988. The bottom panels (e) and (f) denote the difference between the observed and balanced (nondivergent) winds at 850 and 400 mb, respectively. The low-level convergence and upper-level divergence near Newfoundland dominate the vector difference fields, indicating that the observed nondivergent flow is adequately captured by the streamfunction solution to the balance equations. It is also possible to recover much of the observed divergence field through an iterative procedure. Starting with no vertical motion, the EPV is advected by the nondivergent wind, the flow tendencies are computed, the irrotational and vertical motions deduced (accounting for the effects of condensation) and used to improve the estimate of the EPV advection and the generation of EPV by latent heat release. The process is repeated until we converge upon a solution for the EPV tendency, vertical motion, and divergence. Details of the procedure appear in appendix B. Figure 3 shows the irrotational horizontal winds and vertical velocities calculated by this method. Comparing Figs. 3a and 3b with 2e and 2f, we note that about half of the maximum irrotational wind at low levels and most of the magnitude at upper levels is recovered. The spatial pattern of the wind fields differs most at upper levels. Because of uncertainties in the NMC analysis of divergence itself, it is difficult to explain the differences between these fields. A better test for our method of diagnosing divergence and vertical motion would be to use forecast model data from which dynamically consistent fields are available.

This example indicates the ability of the balanced flow to accurately represent the observed flow, even in situations where the traditional Rossby number is not small (the relative vorticity at the cyclone center in Fig. 2a was nearly twice the Coriolis parameter). The strength of this approach is its accuracy in highly curved flows and that it can be used to invert a nearly exact form of Ertel's PV.

c. *Inversion of EPV perturbations*

Piecewise inversion of PV is perhaps the most useful diagnostic application of the invertibility principle. When the invertibility relation is linear, piecewise inversion is a Green's function technique, for one can imagine inverting an array of point source PV anomalies whose circulations sum to the total flow (Pedlosky 1979, p. 102). A breakup of the flow ad infinitum is not our goal here. Rather, we seek the minimum number of dynamically significant perturbations that adequately describe a cyclone development. This is a generalization of HMR's description of baroclinic instability as two counterpropagating, interacting Rossby waves. By calculating the balanced winds associated with individual PV anomalies, we can deduce which anomalies figure prominently in the amplification of others.[6] We can also diagnose developments in which the PV anomalies are not growing, but are merely changing their relative positions or their shapes. In addition, the conservation law for EPV will help isolate those disturbances growing chiefly by nonconservative processes while the invertibility principle allows direct calculation of their associated circulations. For PPV such calculations are straightforward, once one identifies perturbations, because the invertibility relation is linear. The nonlinearities occurring in (2.1) and (2.3) complicate the piecewise inversion of EPV. We discuss this problem below in detail.

First, we must define the perturbations. In most of the published inversions of EPV (e.g., Eliassen and Kleinschmidt 1957; HMR; Thorpe 1986), anomalies were isolated and had idealized structure. In these cases, the perturbation was easily distinguished. Defining perturbations in the atmosphere is a more difficult task. Usually, cyclone systems are identified with temporal filtering techniques ranging in sophistication from simple 12 h changes to bandpass filters. We adopt a middle-of-the-road complexity, defining a perturbation

---

[3] These levels are 1000, 850, 700, 500, 400, 300, 250, 200, 150, and 100 mb.

[4] The lower boundary, as always, complicates our calculations. Because 850 mb is our lowest interior level everywhere, we often require data below the earth's surface in order to calculate PV. In the NMC dataset, temperatures below the surface were obtained by downward extrapolation based on the static stability just above the ground. This produced temperatures below the surface not hydrostatically consistent with the geopotential field (the latter being obtained from a standard atmosphere lapse rate). For consistency with the lower boundary θ distribution, we compute the static stability at the lowest level using the geopotential field. We also use the heights to obtain the stabilities at any grid point where the level below is underground. Use of a standard temperature profile to produce heights below ground implies that the temporal variation of PV at subsurface levels is small (winds below ground were used unaltered).

[5] The midpoint of a level is the layer-average Exner function.

[6] Robinson, 1989, has performed detailed piecewise inversion for the Charney and Green models of baroclinic instability.

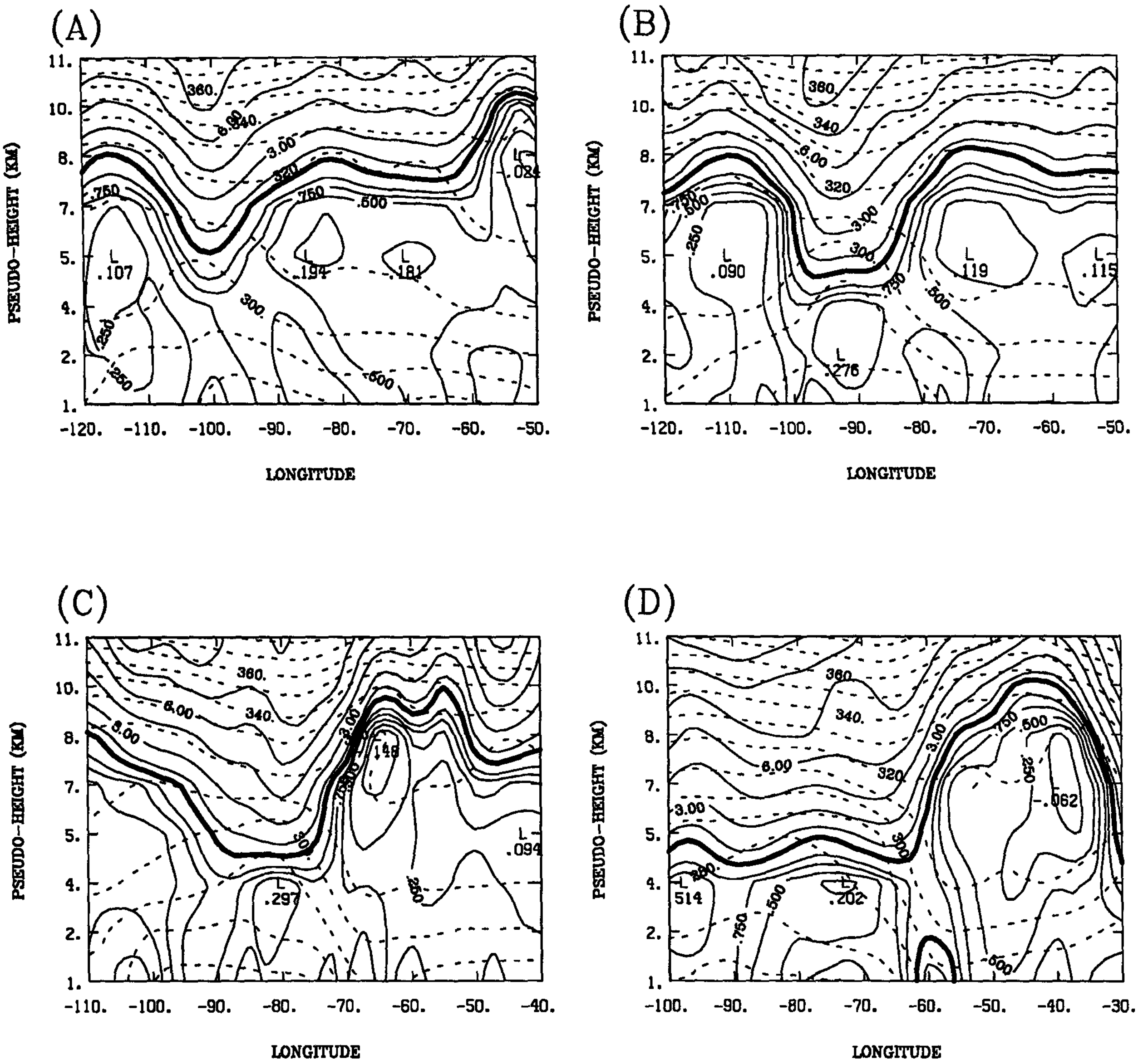

FIG. 5. Cross sections of EPV and potential temperature. Data are at mandatory levels from 850 to 150 mb. The vertical coordinate on these plots is approximate "pseudoheight," defined by $z = (p_0/\rho_0 \kappa g)[1 - \pi(p)/C_p]$ as in Hoskins and Bretherton (1972). EPV contours are at 0.0, 0.25, 0.5, 0.75, 1.5, 3.0, 4.5, 6.0, 7.5, and 9.0 PVU (1.5 is bold line); θ is contoured in 10 K intervals. (a) 0000 UTC 4 February at 42.5°N; (b) 1200 UTC 4 February at 42.5°N; (c) 0000 UTC 5 February at 42.5°N, and (d) 1200 UTC 5 February 1988 at 47.5°N.

as the departure from a time average. Perhaps the best choice is the mean over one synoptic-scale wave period, for instance, the time interval between cyclones at any location (or a multiple of that time). It is not always easy to determine such a period and its validity is usually constrained geographically.

Assuming a time mean can be reasonably defined, we wish to compute a balanced mean state. We formally decompose the EPV into mean and perturbation parts; $q(\lambda, \phi, \pi, t) \equiv \bar{q}(\lambda, \phi, \pi) + q'(\lambda, \phi, \pi, t)$ and do the same for Φ and Ψ. These definitions are inserted into (2.1) and (2.3) and the terms involving only mean quantities are grouped together. The mean equations are identical to (2.1) and (2.3) except all dependent variables are mean values. We average q and boundary θ in time, then invert for the balanced mean flow.[7] The perturbation fields can then be calculated and they satisfy the (nonlinear) perturbation equation by defini-

---

[7] The time-mean values of Ψ and Φ serve as lateral boundary conditions.

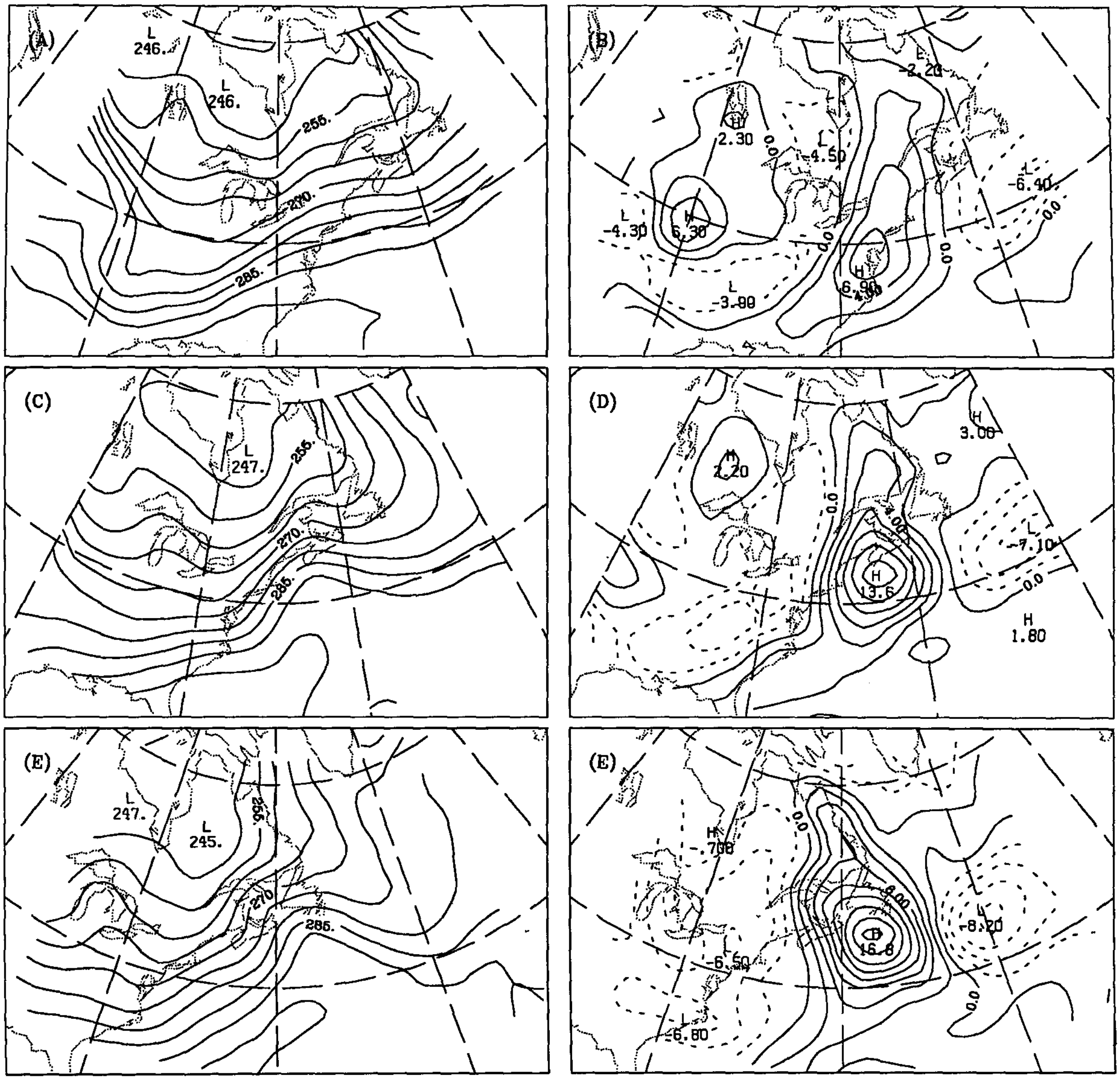

FIG. 6. Lower boundary potential temperature, full field (contour interval 5 K) and perturbations (contour interval 2 K). Panels (a) and (b) are for 1200 UTC 4 February, (c) and (d) for 0000 UTC 5 February, and (e) and (f) for 1200 UTC 5 February 1988.

tion. However, we require linear equations for our piecewise inversion of perturbation EPV. As an alternative to dispensing with the nonlinear terms altogether, we perform the linearization by hiding the nonlinear terms in the nonconstant coefficients of the linear differential operator.

To illustrate this, consider a simple system, $q(t) = A(t)B(t)$ along with some other relation between A and B. Proceeding as outlined above, the equation for q' is

$$q'(t) = \bar{A}B'(t) + \bar{B}A'(t) + A'(t)B'(t). \qquad (2.5)$$

Now partition the q' field into N parts; $q'(t) = \Sigma_{n=1}^{N} \times q_n$ and do the same for A' and B'. Substitution of these summations into (2.5) will result in the linear terms plus a series of cross terms

$$\sum_{n=1}^{N} q_n = \bar{A} \sum_{n=1}^{N} B_n + \bar{B} \sum_{n=1}^{N} A_n + A_1B_1 + A_1B_2 + A_2B_1 + \cdots + A_NB_N. \qquad (2.6)$$

It is not obvious how to generate a series of equations relating each q_n uniquely to an A_n and B_n. Two extreme choices for partitioning are

$$\begin{aligned} q_n &= \bar{A}B_n + \bar{B}A_n + A_n(B_1 + B_2 + \cdots + B_N) \\ &= \bar{A}B_n + BA_n \end{aligned} \qquad (2.7)$$

and

$$q_n = \bar{A}B_n + \bar{B}A_n + B_n(A_1 + A_2 + \cdots + A_N)$$
$$= AB_n + \bar{B}A_n. \qquad (2.8)$$

We choose the average of these, that is,

$$q_n = \left(\bar{A} + \frac{1}{2}\sum_{n=1}^{N} A_n\right)B_n + \left(\bar{B} + \frac{1}{2}\sum_{n=1}^{N} B_n\right)A_n, \qquad (2.9)$$

the only choice possessing the symmetry of invariance under an exchange of A and B. Following this procedure, we obtain the perturbation forms of (2.1) and (2.3):

$$\nabla^2\Phi_n = \nabla\cdot(f\nabla\Psi_n) + \frac{2}{a^4\cos^2\phi} \times\left(\frac{\partial^2\Psi^*}{\partial\lambda^2}\frac{\partial^2\Psi_n}{\partial\phi^2} + \frac{\partial^2\Psi^*}{\partial\phi^2}\frac{\partial^2\Psi_n}{\partial\lambda^2} - 2\frac{\partial^2\Psi^*}{\partial\lambda\partial\phi}\frac{\partial^2\Psi_n}{\partial\lambda\partial\phi}\right) \qquad (2.10)$$

and

$$q_n = \frac{g\kappa\pi}{p}\left[(f+\nabla^2\Psi^*)\frac{\partial^2\Phi_n}{\partial\pi^2} + \frac{\partial^2\Phi^*}{\partial\pi^2}\nabla^2\Psi_n - \frac{1}{a^2\cos^2\phi}\left(\frac{\partial^2\Psi^*}{\partial\lambda\partial\pi}\frac{\partial^2\Phi_n}{\partial\lambda\partial\pi} + \frac{\partial^2\Phi^*}{\partial\lambda\partial\pi}\frac{\partial^2\Psi_n}{\partial\lambda\partial\pi}\right) - \frac{1}{a^2}\left(\frac{\partial^2\Psi^*}{\partial\phi\partial\pi}\frac{\partial^2\Phi_n}{\partial\phi\partial\pi} + \frac{\partial^2\Phi^*}{\partial\phi\partial\pi}\frac{\partial^2\Psi_n}{\partial\phi\partial\pi}\right)\right], \qquad (2.11)$$

where $[\ ]^* = [\bar{\ }] + \frac{1}{2}\sum_{n=1}^{N}[\ ]_n$. Equations (2.10) and (2.11) form a linear system for the flow perturbations Ψ_n and Φ_n associated with any perturbation of EPV, q_n. Although the nonlinearities present in (2.1) and (2.3) imply a certain arbitrariness to the way we partition the EPV, we emphasize that (2.10) and (2.11) may represent the least arbitrary approach.

The upper and lower boundary conditions are simply $(\partial\Phi_n/\partial\pi, \partial\Psi_n/\partial\pi) = -\theta_n$ at $\pi = \pi_T$ and $\pi = \pi_0$. Appropriate conditions for the lateral boundaries are difficult to determine because the contribution from individual anomalies of EPV to the flow at any point is not known a priori. Our approach is simply to choose a domain much larger than the region of interest and apply homogeneous lateral boundary conditions for each Ψ_n and Φ_n. An alternative would be to invert the EPV over a global domain (or at least a hemisphere), although this is unnecessarily costly.

3. Case study

a. Structure

In this section, a case of cyclogenesis is presented to illustrate the application to observations of the PV diagnostics we have described. Many cases must be considered to assemble a consistent conceptual picture of cyclone development. Here, we only wish to show what insights are obtainable from the diagnostics developed in the previous section.

The case, which occurred on 4 and 5 February 1988 over eastern North America, was an example of rapid cyclogenesis with a maximum sea-level pressure fall of about 30 mb in 24 h (Fig. 4). The midtropospheric height charts show a rather small amplitude synoptic-scale wave pattern which grows considerably by 1200 UTC 5 February.

To obtain dynamical insight from our piecewise inversion diagnostic, we would like to objectively identify EPV disturbances with individual dynamical significance. These may be Rossby waves at different latitudes or altitudes, for instance. Emphasis on the vertical structure of perturbations in both simple theoretical models and synoptic description of cyclogenesis suggests examining the flows associated with EPV anomalies at different levels. Figure 5 presents vertical cross sections of EPV and potential temperature during the cyclogenesis period. At 0000 UTC 4 February, we see a fairly weak upper-level wave pattern, marked by undulations in the tropopause [defined as the 1.5 potential vorticity unit (PVU)[8] contour]. There is also an EPV disturbance in the lower troposphere, with positive perturbations near 85° and 55°W. As time proceeds, the westernmost lower-tropospheric positive perturbation achieves a magnitude of over two potential vorticity units (2 PVU) by 1200 UTC 5 February, while there is a rapid amplification of the upper-level ridge downstream. A similar structure was also noted by Hoskins and Berrisford (1988) for the eastern Atlantic storm of October 1987. Because this last cross section is taken farther north than the others, the large-scale polar vortex, with its low tropopause, is quite apparent in the left half of the figure. This suggests that one significant EPV disturbance is intimately linked with wavelike variations in the tropopause position and another is concentrated in the lower troposphere, within the frontal zone.

To quantify our mean and perturbation definitions, the mean state for this case is defined as the time average between 1200 UTC 3 and 0000 UTC 8 February, plus a slowly varying function that accounts for the trend in the mean state between these two times. Most of the trend is associated with the slow evolution of the planetary-scale upper-level polar vortex. The time dependence of the mean is $A(\lambda, \phi, \pi)\cos[\pi(t - t_0)/\tau]$, where τ is 5 days, t_0 is 1200 UTC 3 February and A is determined by a spectral decomposition in time at each grid point. Because we are allowing the mean EPV and boundary θ to vary, we must perform an inversion at each time to obtain the evolving balanced mean flow.

Shown in Fig. 6 is the evolution of total and perturbation θ_B (hereafter referred to as "surface" θ). The

---

[8] 1 PVU = 10^{-6} m^2 K kg^{-1} s^{-1}. A typical tropospheric value is 0.5 PVU; stratospheric values are roughly an order of magnitude larger.

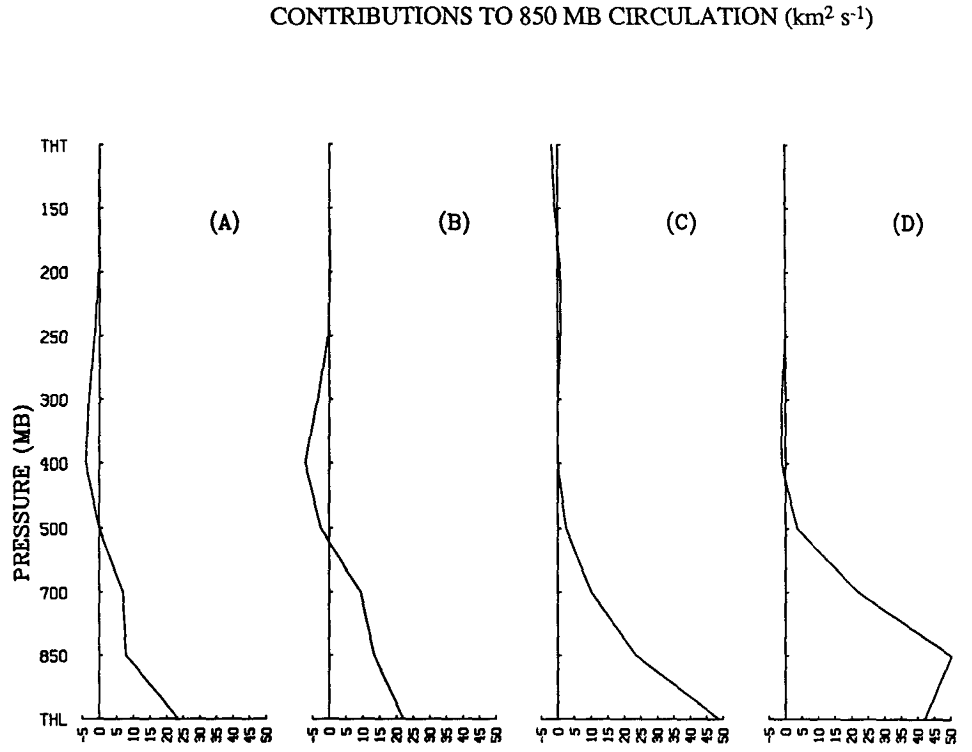

EPV 1200 UTC 04	PPV 1200 UTC 04	EPV 1200 UTC 05	PPV 1200 UTC 05
θ_B contrib. = 23	θ_B contrib. = 22	θ_B contrib. = 49	θ_B contrib. = 42
850 mb and up = 6	850 mb and up = 10	850 mb and up = 35	850 mb and up = 74

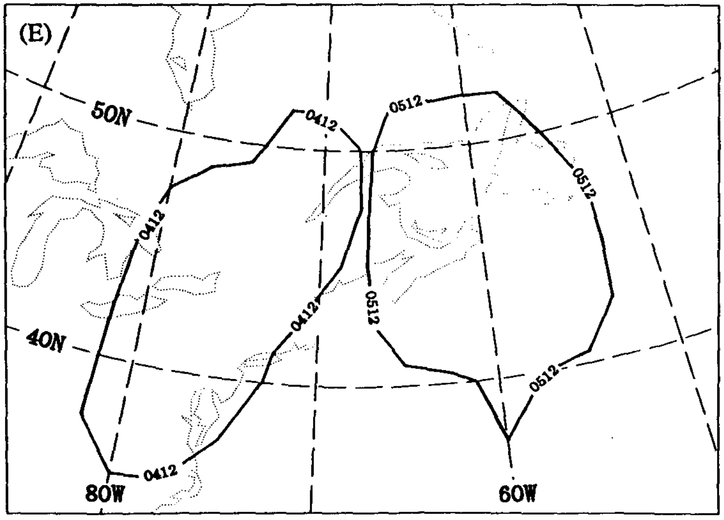

FIG. 7. Profile of contributions to the circulation at 850 mb. THL denotes θ_B perturbations; THT denotes θ perturbations at the upper boundary (125 mb). The contribution from θ_B anomalies and the contribution from everything except θ_B anomalies are both printed below each graph. Panels (a) and (b) result from EPV and PPV inversions, respectively at 1200 UTC 4 February; (c) and (d) are as (a) and (b), but for 1200 UTC 5 February 1988. Panel (e) is a map indicating the regions of integration at each time (these were the same for the EPV and PPV calculations). The contour labeled 0412 shows the integration area at 1200 UTC 4 February; the contour labeled 0512 depicts the integration area at 1200 UTC 5 February. See text for definition of these areas.

perturbation structure is meridionally elongated and rather frontal in character at 1200 UTC on the 4th. The positive anomaly achieves its largest magnitude 24 h later, exceeding 16°C, while a cold perturbation of smaller magnitude covers much of the eastern United States. The southward deflection of isotherms in the lee of the Rockies is a rather persistent feature during this time period, hence, it does not appear as a perturbation by our definition.

To compare relative contributions to the perturbation flow, we perform three-dimensional inversions of θ_B and individual levels of EPV anomalies by solving (2.10) and (2.11) using standard successive overrelaxation. When inverting interior EPV anomalies, we apply a homogeneous condition on both horizontal boundaries. The boundary θ anomalies are inverted separately by setting $q_n = 0$ in (2.11) everywhere in the interior. We examine the solution to each inversion at the same level, 850 mb (our lowest interior level), in order to assess the relative contributions to the low-level cyclone circulation. For comparison with the EPV inversions, we have also inverted PPV anomalies using (1.2).[9]

To quantify the contributions to the low-level cyclone circulation, we integrate the 850-mb vorticity associated with individual levels of perturbation PV (and separately, θ_B) over the area of positive total perturbation vorticity ζ' around the cyclone center.[10] Figure 7 displays the contributions to the 850-mb cyclonic circulation from each level of perturbation EPV at two times, 1200 UTC on the 4th and 5th. To obtain each point on a curve, the system (2.10) and (2.11) was solved with either $q_n = q'$ at one level ($\theta_n = 0$ on the horizontal boundaries) or $\theta_n = \theta'$ on one of the horizontal boundaries ($q_n = 0$ in the interior). The areas of integration for both times are also shown in Fig. 7. As expected from scaling arguments, agreement between the EPV and PPV inversions is quite good in the early stages of the cyclone. At 1200 UTC on the 4th, there is low-PV air aloft, whose reflection at low levels tends to cancel the circulation from the positive θ_B perturbation and the positive low-level PV anomaly. By 1200 UTC on the 5th, there is almost no contribution from the upper troposphere. At this time, the lower PV has become quite important and the EPV and PPV inversions now differ more, to the point of qualitatively changing the shape of the profile. The lower-troposheric EPV contributes about 42%, while the low-level PPV represents about 64% of the geostrophic circulation. These differences are not related to the difference between real vorticity and geostrophic vorticity. A similar result is found if we compare the contribution to the 850-mb geostrophic circulation in the EPV inversion with the PPV calculation.

Intense low-level EPV anomalies have been observed in other cyclones as well (Manabe 1956; Eliassen and Kleinschmidt 1957; Boyle and Bosart 1986; Whitaker et al. 1988; Kuo and Reed 1988; Hoskins and Berrisford 1988; Kuo et al. 1990b). In each of these other cases, the air within this low-level EPV anomaly was not of stratospheric origin and the EPV anomalies were probably generated by condensation. In section 3b we shall present evidence pointing to the same conclusion. Therefore, it seems that the EPV anomaly at low levels constitutes a distinct, dynamically significant perturbation. Upper-level EPV and surface θ perturbations have their own dynamical significance because they are each embedded within actual or effective gradients of potential vorticity, namely, the gradient at the tropopause and the gradient in the surface θ field, respectively.

We suggest a possibly illuminating partitioning of the total EPV perturbation field into three anomalies; upper-level EPV (500 mb and above, denoted UPV), lower EPV (850 and 700 mb, denoted LPV), and θ_B. Figure 8 shows the evolution of 850-mb vorticity associated with these three anomalies over a 24-h period beginning 1200 UTC on the 4th. The low-level signature of each of these perturbations grows with time. The lower EPV and θ_B anomalies are nearly collocated, although there is some suggestion that the lower EPV is slightly upshear early on. We also note that the low-level signature of the upper EPV perturbation has amplified by 1200 UTC on the 5th, especially in the anticyclonic phase. Thus, although the upper EPV does not contribute directly to the cyclonic vortex circulation, its signature at low levels is significant and, as we shall show, it was probably important for the development of the low-level potential temperature field.

b. Origin of perturbations

A complete description of this development must also include a discussion of how the significant EPV perturbations were created. We will first discuss the development of θ_B anomalies by horizontal advection. Figure 9 shows the low-level winds associated with the θ_B, lower- and upper-tropospheric EPV perturbations overlayed on the θ_B field. The self-advections of the thermal anomalies act to propagate the temperature wave downshear along the baroclinic zone as a surface Rossby wave. The winds from the interior EPV suggest that these anomalies have a significant role in amplifying the surface thermal wave. To quantify this, we first calculate the tendencies of 850-mb vorticity resulting from advection of θ_B by the winds from each of the three perturbations. Then we compute the area-integrated enstrophy tendency, by correlating the vorticity tendencies with the vorticity of the thermal per-

---

[9] The PPV fields here were calculated from the balanced heights rather than observed heights. This simply eliminates most of the noise in PPV derived from analyzed heights.

[10] Another constraint on the integration region is that the perturbation vorticity must decrease away from its maximum value near the low center.

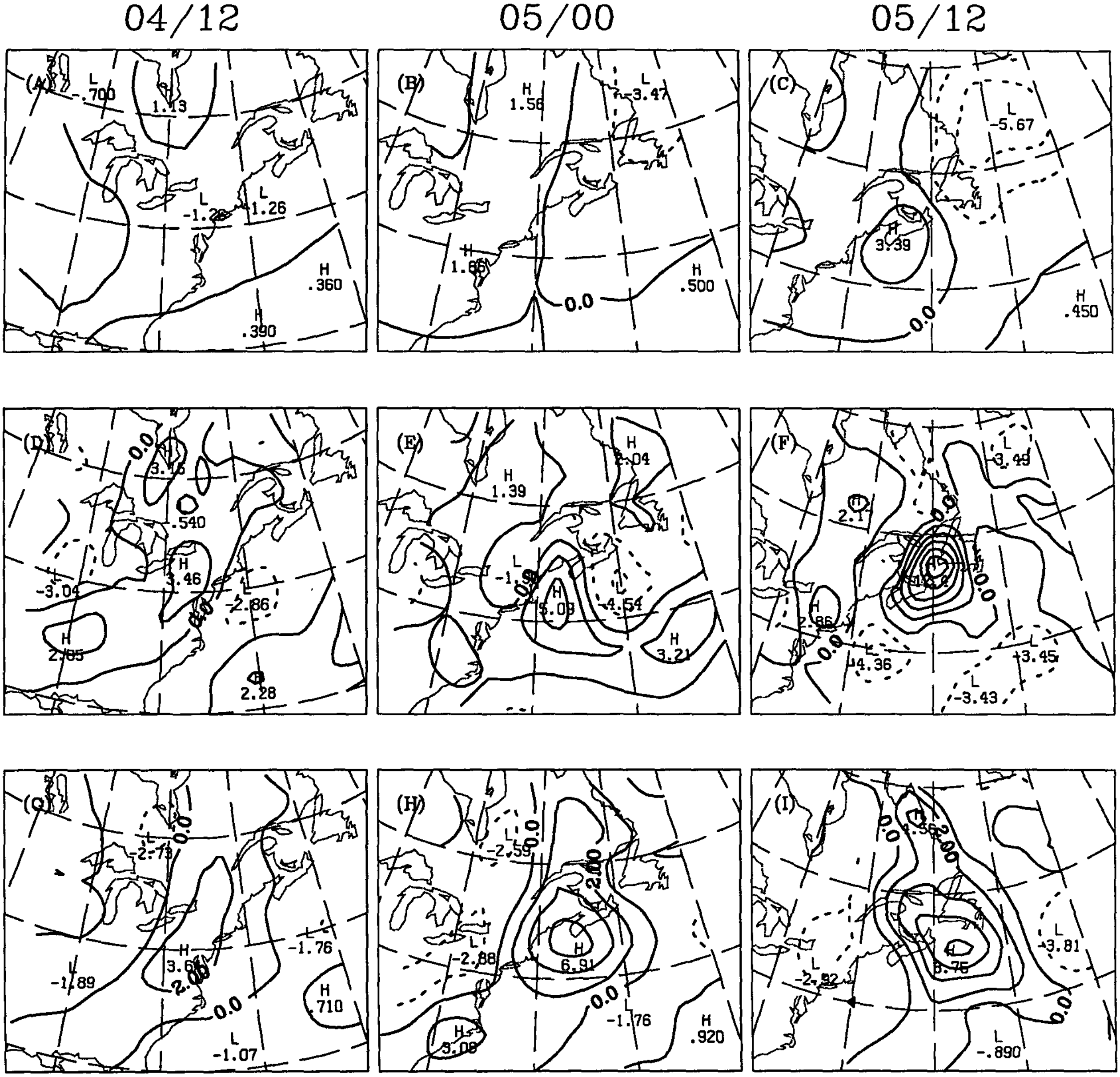

FIG. 8. Evolution of the vorticity at 850 mb associated with boundary θ, lower EPV (q at 850 and 700 mb), and upper EPV (q at 500 mb and up). Bottom row is θ, middle row is lower-level EPV, and top row is upper-level EPV. Contour interval is 2×10^{-5} s^{-1}; dashed contours denote negative perturbation vorticity.

turbations (and dividing by 2). Each domain is 20° lat × 40° long centered at 40°N and near the longitude of the warm anomaly. The numbers in Table 1 have been normalized by the area-integrated enstrophy associated with the θ_B perturbations and, therefore, have the dimensions of inverse time.

At 1200 UTC on the 4th, the 850-mb enstrophy tendency resulting from the UPV anomalies is due to cold advection east of 65°W that is in phase with negative perturbation temperatures. It is likely that these tendencies would be reduced by sensible heat fluxes from the underlying ocean. In general, these calculations bear out the impression from Fig. 9 that the lower EPV amplifies the thermal wave early on; the upper EPV becomes important later.

Because of the phase tilt between the upper and lower anomalies, one may ask whether a mutual intensification process is taking place, in which the circulation associated with the lower EPV and surface θ perturbations is amplifying the upper disturbance. To investigate this, we consider the circulation of the lower EPV and surface θ anomalies together. As a further simpli-

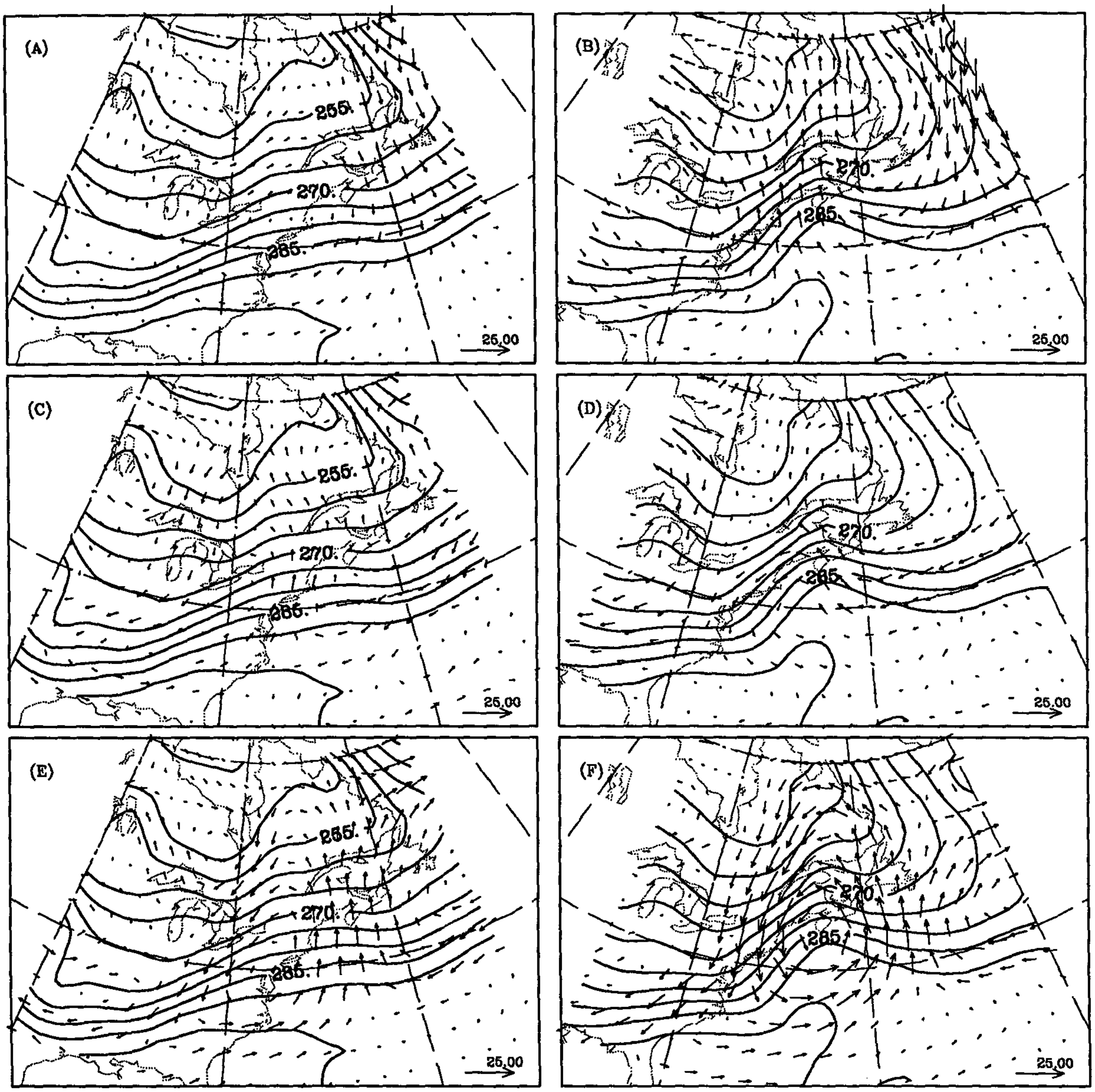

FIG. 9. Nondivergent winds at 925 mb (average of 1000 and 850 mb) overlayed on θ (contour interval 5 K) at the lower boundary. Panels (a), (c), and (e) depict winds from upper EPV, lower EPV, and boundary θ perturbations, respectively, for 1200 UTC 4 February. Panels (b), (d), and (f) are as in (a), (c), and (e) but for 0000 UTC 5 February.

fication, we represent the upper-level disturbance on a map of tropopause potential temperature, i.e., θ on a surface of constant EPV. The usefulness of this representation stems from the observation that isentropic surfaces making the transition from the troposphere to stratosphere usually feature a sharp gradient of EPV between the two air masses. The upper-tropospheric waves are intimately associated with excursions of this transition region from its mean position. Much of the information on an isentropic surface is thus contained in the location of this EPV gradient (Danielsen 1968). Therefore, within this gradient, we select a single EPV surface (1.5 PVU), which defines the tropopause, and create a map of tropopause potential temperature by interpolating θ onto that surface. This is the counterpart of lower boundary potential temperature, except that the tropopause is flexible, and it is a material surface when EPV and θ are conserved. Troughs and ridges are represented on the tropopause by "cold" and "warm" anomalies, respectively (Fig. 5).[11]

An example of the relationship between isentropic EPV and tropopause maps is presented in Fig. 10.

---

[11] "Cold" and "warm" refer to potential temperature, but the actual temperature anomalies on the tropopause may have the opposite signs.

TABLE 1. Normalized enstrophy tendencies are in units of 10^{-5} s^{-1}.

Time	θ_B	LPV	UPV
1200 UTC 4 February 1988	0.1	1.5	0.8
1200 UTC 5 February 1988	0.1	1.8	1.9

Shown are the 290 and 320 K maps of EPV as well as θ on the 1.5-PVU surface at 1200 UTC 5 February. The tropopause map neatly consolidates the information on isentropic charts of EPV except where $\theta(q)$ becomes multivalued, such as in tropopause folds or intense low-level EPV anomalies (as near Newfoundland in Fig. 10a). At such locations, we choose the highest value of θ on the 1.5-PVU surface to represent the tropopause potential temperature and interpolate winds to that level accordingly. Thus, with our method, folds in the tropopause and lower-tropospheric EPV features are absent from tropopause maps, but present on isentropic charts of EPV.

Figure 11 illustrates the combined tropopause winds associated with the low-level EPV and θ_B perturbations on tropopause potential temperature θ_{TR}. The winds from the lower anomalies are apparently amplifying the tropopause wave. The time scale for the deformation of the main gradient of potential temperature into an "S" shape by 0000 UTC on the 6th is roughly consistent with the advective time scale implied by the plotted winds. The timing of this coincides with the amplification of the lower boundary potential temperature wave by the upper EPV disturbance. Hence, this cyclogenesis may be partly conceptualized as a mutual interaction of tropopause and surface Rossby waves, although the low-level EPV anomaly apparently enhanced the growth of the θ_B perturbation as well.

We now consider the origin of the low-level EPV perturbation. Figure 10a depicts this feature as an isolated EPV maximum on an isentropic surface at 1200 UTC 5 February, suggesting a nonconservative origin. Processes such as condensation, evaporation, radiation, and friction (including turbulent mixing) can act to generate extrema of isentropic EPV. However, the anomaly may be connected with the stratospheric air to the west by a thin filament of high EPV unresolved by our data. Therefore, this isentropic map is insufficient to rule out advection completely.

The air near the center of the anomaly is saturated, as indicated by the observation from Stephensville, Newfoundland (YJT), at 1200 UTC 5 February in Fig. 12. This figure shows wind, pressure, and relative humidity on the 290 K surface of saturation equivalent potential temperature (θ_e^*). The quantity $\theta_e^* = \theta \times \exp(L_v w_s / C_p T)$ is a thermodynamic state variable conserved for reversible motion in saturated air. Here, L_v is the latent heat of vaporization ($=2.51 \times 10^6$ J kg^{-1}) and w_s is the saturation mixing ratio. We could use θ_e as our thermodynamic variable instead of θ_e^*. Under saturated conditions these are identical, but we use θ_e^* because of uncertainties in relative humidity measurements, even near saturation. By performing a back trajectory on this θ_e^* surface, starting at YJT on the 5th at 1200 UTC, we estimate that the air originated just north of ship *KHRH* (*KHR* on bottom figure) 12 h earlier. Therefore, the EPV anomaly has no direct link to the stratospheric air to the west, and an apparent absence of high EPV values to the southeast of the storm at 0000 UTC 5 February rules out an advective origin altogether. In addition, 12-h precipitation totals at stations in Nova Scotia exceeded 1 in, suggesting that condensation is the generation mechanism that produced the anomaly.

To be more quantitative, one can estimate the EPV generation rates from latent heat release using two methods. Both assume an absence of upright convective instability, which is substantiated by soundings and a

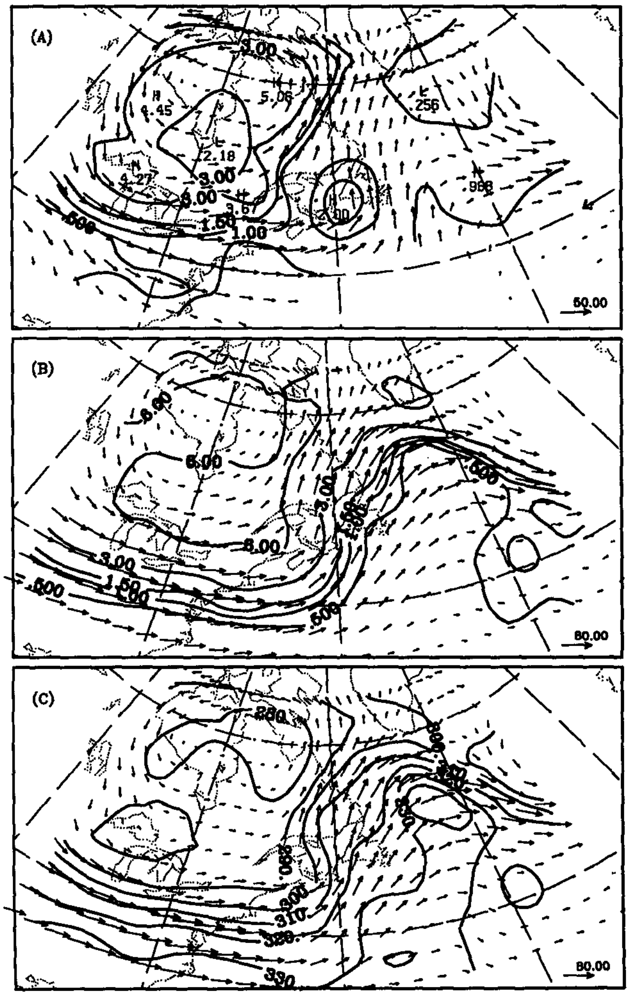

FIG. 10. (a) 290 K EPV map for 1200 UTC 5 February, EPV contours are 0.5, 1.0, 1.5, and 3.0 PVU. Plotted data extend from 35° to 65°N and 95° to 30°W; (b) as in (a) but for 320 K; (c) tropopause potential temperature and winds, contour interval 10 K.

lack of convective showers reported at the surface. The first method uses the solution to the balanced ω equation (appendix B), with latent heat release allowed in regions of saturated ascent (incorporated as locally reduced static stability), to calculate $d\theta/dt$ and then EPV generation from

$$\left(\frac{dq}{dt}\right)_{\mathrm{LH}} = \frac{g\kappa\pi}{p}\,\eta\cdot\nabla\left(\frac{d\theta}{dt}\right)_{\mathrm{LH}}, \tag{3.1}$$

where the subscript LH refers only to condensational heating. The regions of reduced static stability are initially unknown and are found by iteration during the ω-equation inversion. Note that we include horizontal gradients of heating in this calculation, which can be significant in frontal zones. In addition, the nonconservative generation term is free to feed back on the flow tendency and vertical velocity.

For the second estimate of the EPV generation rate, we make use of the reported accumulated precipitation at surface observing stations. By equating the precipitation rate to the vertically integrated condensation rate we obtain

$$\rho_L L_v P = \int_{\pi_s}^{0} d\pi\left[\frac{p_0}{R_d g}\,\omega^*\theta\gamma\left(\frac{\pi}{C_p}\right)^{2.5}\right], \tag{3.2}$$

where

$$\gamma = \left(1 - \frac{C_pR_vT}{L_vR_d}\right)\left(1 + \frac{C_pR_vT^2}{Q_sL_v^2}\right)^{-1}$$

with ρ_L the density of water, Q_s the saturation specific humidity, $\omega^* \equiv d\pi/dt$, and we neglect the effect of water vapor on the specific heat. The diabatic heating is just $d\theta/dt = -\omega^*\theta\gamma/\pi$. In (3.2), ω^* is the only unknown, although we need another constraint in order to solve for its vertical profile. We assume that ω^* is piecewise linear in $\pi(p)$ with the *level* of its maximum value given by the ω-equation solution (interpolated to the station location). It is then straightforward to solve for the maximum value of ω^* and calculate the diabatic heating profile. We compute the generation of EPV by neglecting the horizontal gradients of heating and using an absolute vorticity interpolated from the gridded data.[12] The resulting EPV generation values are not very sensitive to the imposed level of maximum vertical velocity; the dominant factor for controlling the vertical variation of heating is the rapid decrease with height of saturation mixing ratio.

To estimate the EPV generation at a time t_0, we require the precipitation rate at t_0. For stations reporting precipitation at t_0, we used the 6-h rainfall total (or liquid equivalent in the case of frozen precipitation) centered on that time. Hourly observations were used to determine the duration of the precipitation if it was less than 6 h.

In Fig. 13 we display EPV generation rates obtained from both methods outlined above. Figures 13a and 13c show $(dq/dt)_{LH}$ obtained from inverting the prognostic balance equations that incorporate moist static stability, overlayed on 850-mb EPV for 1200 UTC on the 4th and 5th, respectively; Figs. 13b and 13d are maps of the generation rates (in PVU per 12 h) obtained from station precipitation data at times corresponding to Figs. 13a and 13c, respectively. The magnitudes of the rates agree rather well, but the generation regions in Figs. 13b and 13d appear slightly upshear from those in Figs. 13a and 13c. The discrepancy at the latter time likely occurs because we used 6-h synoptic station reports valid at 1200 UTC. In this case, the appropriate t_0 is 0900 UTC. Given that the cyclone's ascent region was translating at roughly 20 m s^{-1}, 3 h corresponds to roughly 200 km upstream from the 1200 UTC position, almost enough to account for the difference in position. At 1200 UTC 4 February, the precipitation at ERI is probably lake enhanced while orography may be influencing totals at CRW. The localized nature of the precipitation at these stations is probably unresolvable by our ω-equation calculations. This, combined with offshore rainfall unrecorded at the surface, apparently displaces the station generation region to the west of the region in Fig. 14a. Overall, however, the agreement between the two EPV generation estimates is encouraging and it implies that condensation in nonconvective precipitation provides a large enough source to account for the presence of the low-level EPV anomaly.

4. Summary and discussion

To provide an overview of this cyclogenesis case, Fig. 14 shows cross sections of contributions to the total perturbation geopotential by the upper- and lower EPV disturbances as well as perturbations of θ_B. At 1200 UTC 4 February (left column), the upper EPV geopotential field is nearly 180° out of phase from the θ_B and lower EPV fields. There is, however, a favorable tilt for development between the lower EPV and θ_B disturbances. Although this lower EPV is located near the steering level of the wave (roughly 800 mb under the jet maximum), the phase shift between the warm phase of the surface θ wave and the positive EPV perturbation is much less than in the classical Charney mode.[13] We have seen that this lower EPV anomaly was probably produced by condensation, perhaps aided by friction at the lower boundary.[14] The important

---

[12] Because we neglect the horizontal gradients of heating, this calculation is most suited for assessing the local extrema of PV generation rates. Especially at 1200 on the 5th, the lack of offshore precipitation reports makes estimating the horizontal gradients of heating very difficult.

[13] The Charney mode phase shift is nearly 130° (Davis 1990).

[14] The nonconservative frictional contribution is $(dq/dt)_{FR} = (1/\rho)\nabla\theta\cdot\nabla\times\mathbf{F}$. If the frictional force is proportional to the velocity,

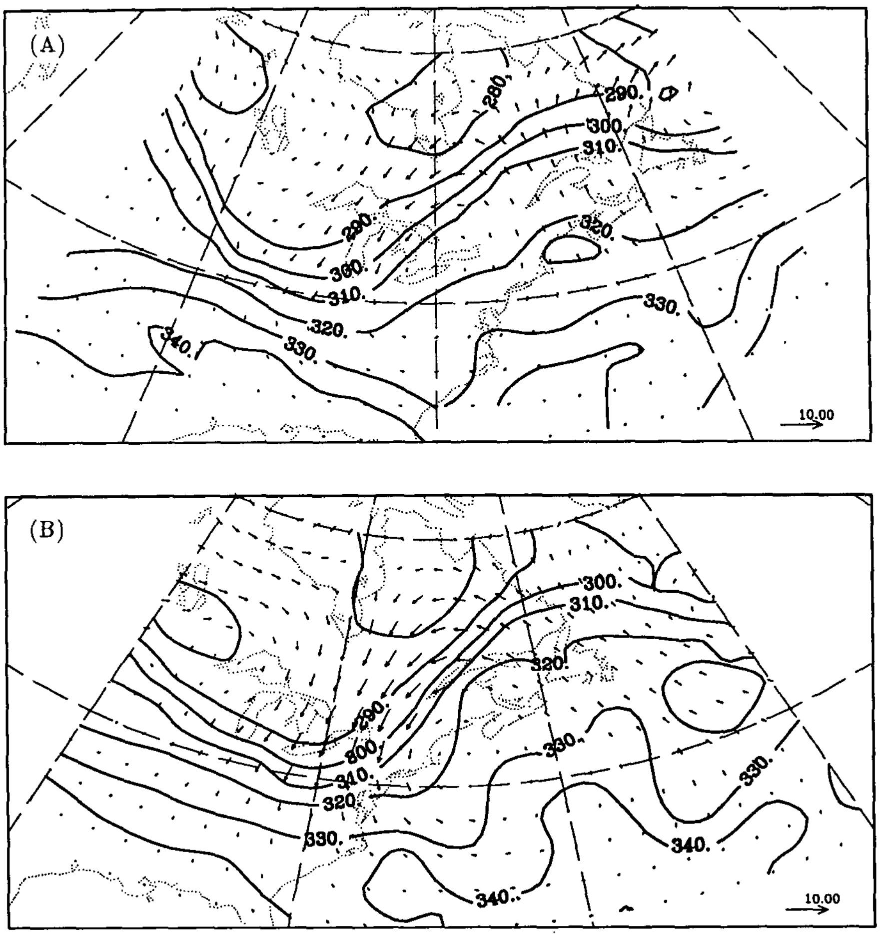

FIG. 11. (a) Tropopause θ and combined winds from lower boundary θ and lower EPV perturbations interpolated to the tropopause, 1200 UTC 4 February; (b) as in (a), but for 0000 UTC 5 February; (c) 1200 UTC 5 February; (d) 0000 UTC 6 February. Contour interval is 10 K. Note change of vector scale in (c) and (d).

point is that the low-level EPV anomaly does not seem to result from advection.

Examining the geostrophic wind perturbations implicit in Fig. 14, we see that the phase shift between the tropopause and lower boundary perturbations decreases with time, attaining a favorable configuration for mutual intensification shortly after 1200 UTC 4 February. The phase shift at 1200 UTC 5 February is roughly 90°, implying possible further growth. However, the upper-level wave structure is rapidly changing at this point (Fig. 11) and the favorable vertical tilt is not maintained long. The lower EPV anomaly is now nearly in phase with the warm lower boundary perturbation and the two circulations add together to enhance the amplification of the upper wave. The flexibility of the tropopause is perhaps crucial to this amplification, since it is quite low in the trough of the upper wave and closer to the ground. The circulation from the lower anomalies is therefore asymmetric when interpolated to this upper surface, tending to amplify the cold phase of the upper wave more rapidly.

Certain aspects of this development resemble the life cycle simulations of Simmons and Hoskins (1978, SH hereafter). Development occurs first at low levels, then upper and lower levels develop simultaneously and, finally, most of the evolution is at upper levels. As shown in Edmon et al. (1980), the initial stage of the SH life cycle resembles a Charney mode. The middle stage is more like an Eady wave in that the PV gradients in the lower troposphere are no longer important. We have already suggested that the initial low-level EPV is probably produced by condensation and the phase relation between the lower EPV and θ differs from a Charney mode. However, work by Montgomery and Farrell (1991) shows that surface Rossby waves may

---

then this term can be an important source of PV on synoptic scales where the relative vorticity is negative and the stability large. Damming of cold air east of the Rockies or Appalachians is such an instance where we may expect friction to create low-level PV.

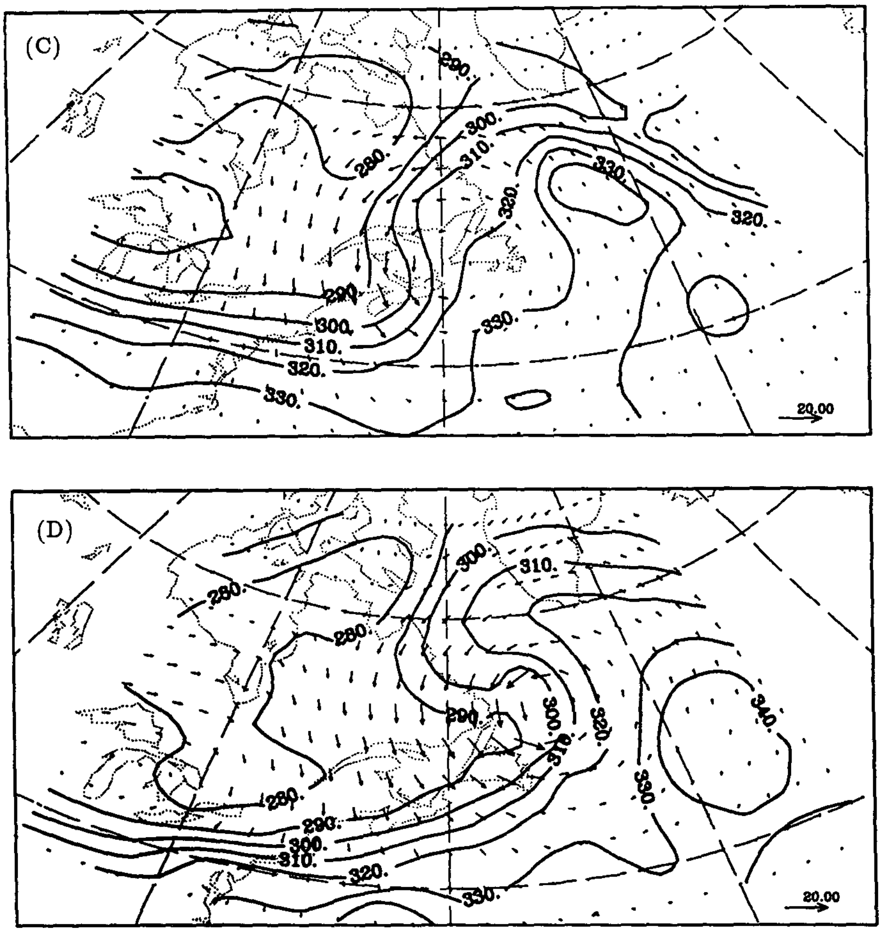

FIG. 11. (Continued)

be destabilized in the presence of moisture. Interior EPV anomalies are produced diabatically, with a resulting vertical structure more in accordance with our observations than classical "dry" solutions. The rapid growth phase is characterized by an interaction of tropopause and lower boundary waves analogous to the Eady model. The main difference between this cyclone and the SH life cycle is the presence of condensation, which probably results in the comparatively rapid evolution in our case. Condensation not only produces a low-level EPV anomaly that adds directly to the low-level cyclone circulation, but also enhances the advection of tropopause potential temperature. In addition, EPV destruction aloft, above the level of maximum latent heating may contribute to the rapid downstream ridge amplification. We have computed EPV destruction rates at upper levels from the ω-equation solution and obtain rates exceeding -1 PVU per 12 h at 400 mb (not shown). Detailed parcel trajectories are probably required to quantify the relative roles of EPV advection and latent heating in the ridge growth.

An alternative perspective of our development through which the simple Eady analogy may be appropriate even in the presence of condensation is to consider moist potential vorticity or saturation potential vorticity in the interior (using θ_e or θ_e^* as the conserved thermodynamic variable) and θ_e or θ_e^* on the horizontal boundaries. The advantage here is that q_e and q_e^* are conserved in saturated air, hence, if the air were saturated and there were no interior moist EPV anomalies initially, there would be none for all time (if friction and all other diabatic heating were absent). Thus, the system would reduce to predicting θ_e or θ_e^* on the horizontal boundaries, conceptually as simple as classical Eady dynamics, However, saturation over an entire baroclinic wave is a highly improbable situation, hence, there will be sources of q_e^* in the dry region that are not necessarily small. In addition, because mixing ratio is not a state variable in unsaturated air, q_e neither obeys Ertel's theorem nor possesses an invertibility principle in the dry region. To have both conservation and invertibility, one must use different forms of EPV in each region. Then, in addition to the upper and lower boundaries, there is an additional boundary at the saturation interface along which θ_e or θ must be specified. This internal boundary is free to

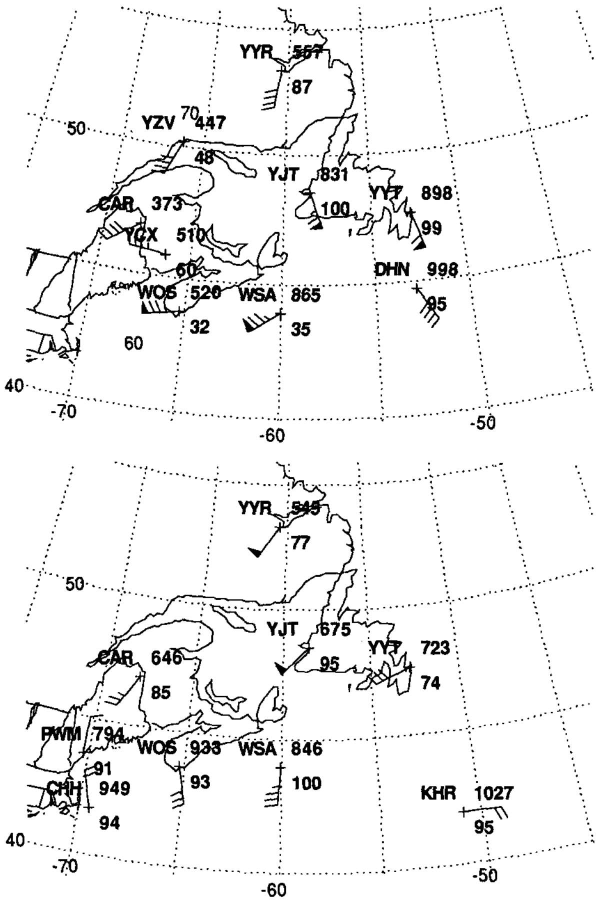

FIG. 12. Observations on the 290 K saturation θ_e surface. The "+" signs indicate the station locations; wind barbs use standard convention in knots. Relative to each "+" symbol, station identification letters appear at upper left, pressure at upper right and relative humidity at lower right. Ship names *DHNE* and *KHRH* have been abbreviated. The dot referred to in text is just above the letters "*KHR*." Top figure is for 1200 UTC 5 February; bottom is for 0000 UTC 5 February.

move in the real atmosphere, rendering the application of the boundary conditions quite difficult and offsetting the possible advantages of this approach.

5. Conclusions and further issues

We have described a diagnostic system for interpreting the behavior of synoptic and larger-scale weather systems based on the conservation and invertibility properties of Ertel's potential vorticity. The conservation property is appealing because it allows one to identify and follow features in a meaningful way and it offers a means to isolate the effects of nonconservative processes on the dynamics. The invertibility property provides a means of quantifying the importance of features in terms of the strength of their associated circulations and their ability to enhance the development of other features.

We have applied these techniques to a particular case of strong extratropical cyclogenesis and have deduced the following: (a) perturbations of potential temperature at the lower boundary accounted for the majority of the cyclone's circulation. (b) A potential vorticity disturbance at low levels was important in the early amplification of the surface thermal wave. Later, an upper EPV disturbance attained a proper phase relationship with the θ_B field to substantially augment its growth. (c) The positive lower EPV anomaly probably resulted from the condensation of water vapor. This feature grew rapidly and eventually contributed about 40% of the low-level cyclonic circulation of the mature storm. (d) The upper wavelike disturbance amplified mostly from advection by the circulations associated with the lower EPV and boundary θ anomalies. This process may be best described as a mutual reinforcement of Rossby edge waves, one at the tropopause, the other at the ground.

We have not dealt with all aspects of this particular case. The upper EPV disturbance did exist in a very weak form prior to development, but we have said little about its ultimate origin. In addition, upper-level frontogenesis that occurred during cyclogenesis was perhaps aided crucially by the circulation associated with the lower-level anomalies (Fig. 11). Tropopause maps are useful for reducing the inherently three-dimensional process of upper-level frontogenesis to two dimensions (on a surface of constant EPV).

Further investigation is needed regarding the total effects of moisture, especially the influence of condensation on the evolution of EPV aloft. Simple considerations suggest that EPV destruction should be occurring above (and downshear from) the level of maximum heating in the upper troposphere. Some of the rapid downstream ridge development may have been due to this process, but it is difficult to say how much from the data we have. Perhaps numerical simulations could help answer this question. In addition, the effect of condensation on the translational speed of the system was not considered quantitatively. Tendency calculations early in the development suggest that the low-level EPV did more to amplify the thermal wave than it did to hasten its progression. However, by 1200 UTC 5 February, the low-level EPV and boundary θ anomalies were more in phase, hence, one would expect an enhanced phase speed.

There are some general issues raised by the above analysis, which may be addressed by investigating a wide range of cyclones, including examples of weak, nondeveloping, and decaying systems in addition to the rapidly developing cyclone studied here. Many cyclones that do not develop nevertheless produce abundant precipitation, and probably large generation rates of EPV. What determines whether low-level EPV anomalies with strong cyclonic circulations will develop? Certainly friction may be important because these EPV anomalies are close to the ground. Also,

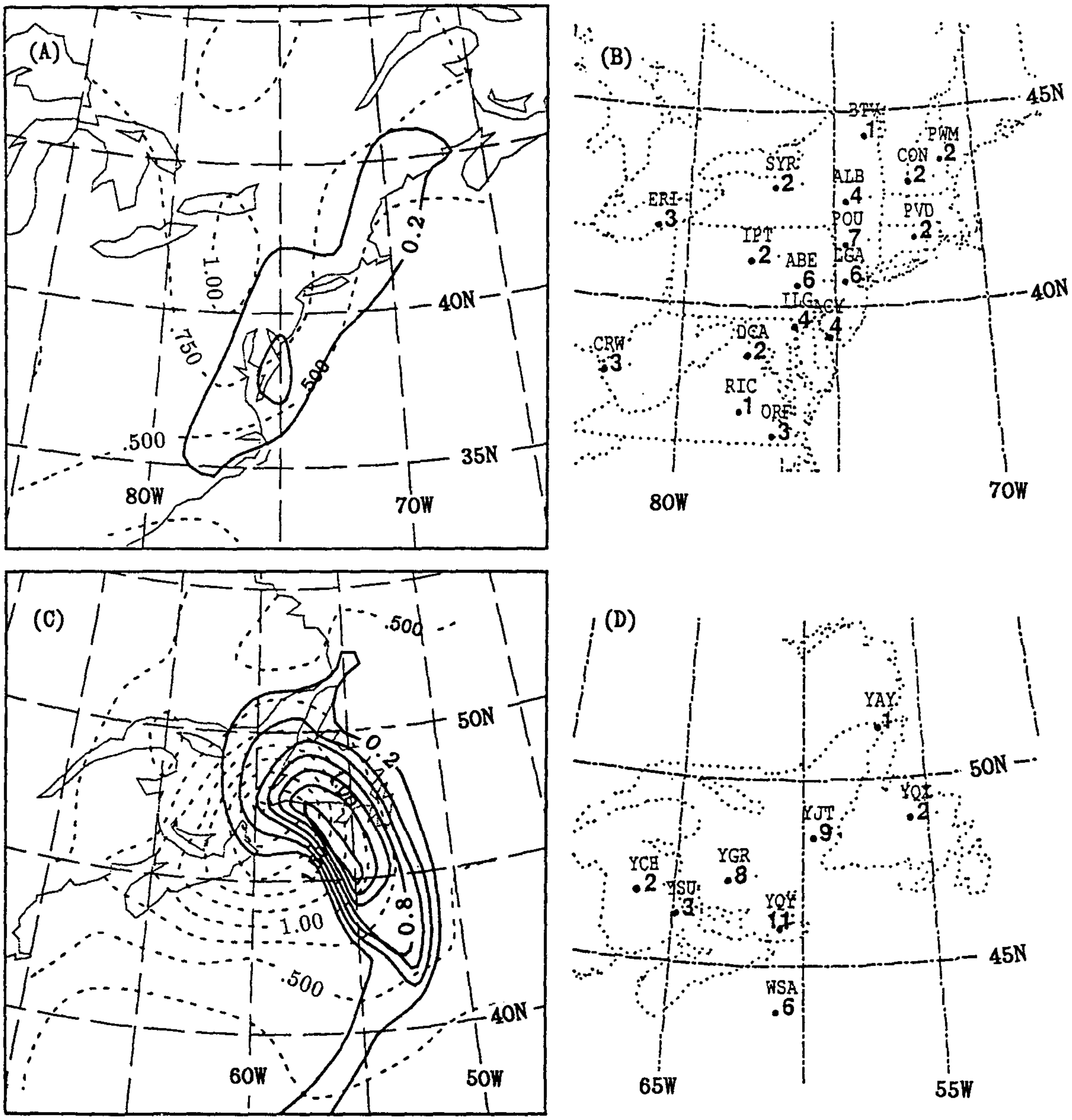

FIG. 13. EPV generation and low-level EPV. Top two figures are for 1200 UTC 4 February. (a) Shows the 850-mb EPV generation rate (contour interval 0.2 PVU per 12 h, solid lines) and 850-mb EPV (contour interval 0.25 PVU, dashed lines); (b) displays EPV generation rates from stations (PVU per 12 h). The corresponding three-letter station code is directly above each number. Panels (c) and (d) are as (a) and (b), except the time is 1200 UTC 5 February. Note that only positive generation rates are contoured in (a) and (c), beginning with 0.2 PVU per 12 h.

deformation is probably very efficient in elongating these EPV anomalies, thereby reducing their associated circulation.

We have been able to describe this development in terms of potential temperature perturbations at the surface and on the dynamic tropopause and potential vorticity anomalies generated by condensation in the lower troposphere. By a process of elimination, we have found that PV anomalies created by advection of tropospheric PV gradients are apparently unimportant. We hypothesize that the tropospheric PV gradients are perhaps being systematically erased by disturbances such that midlatitude dynamics more nearly mimic the "Eady" stage of the SH life cycle than the "Charney" stage. Calculations performed by Robinson (1989) imply that the integrated effect of β dominates the tropopause PV gradient in the Charney model with a tropopause. Our results for the observed case of cyclogenesis studied here are thus not consistent with the Charney model.

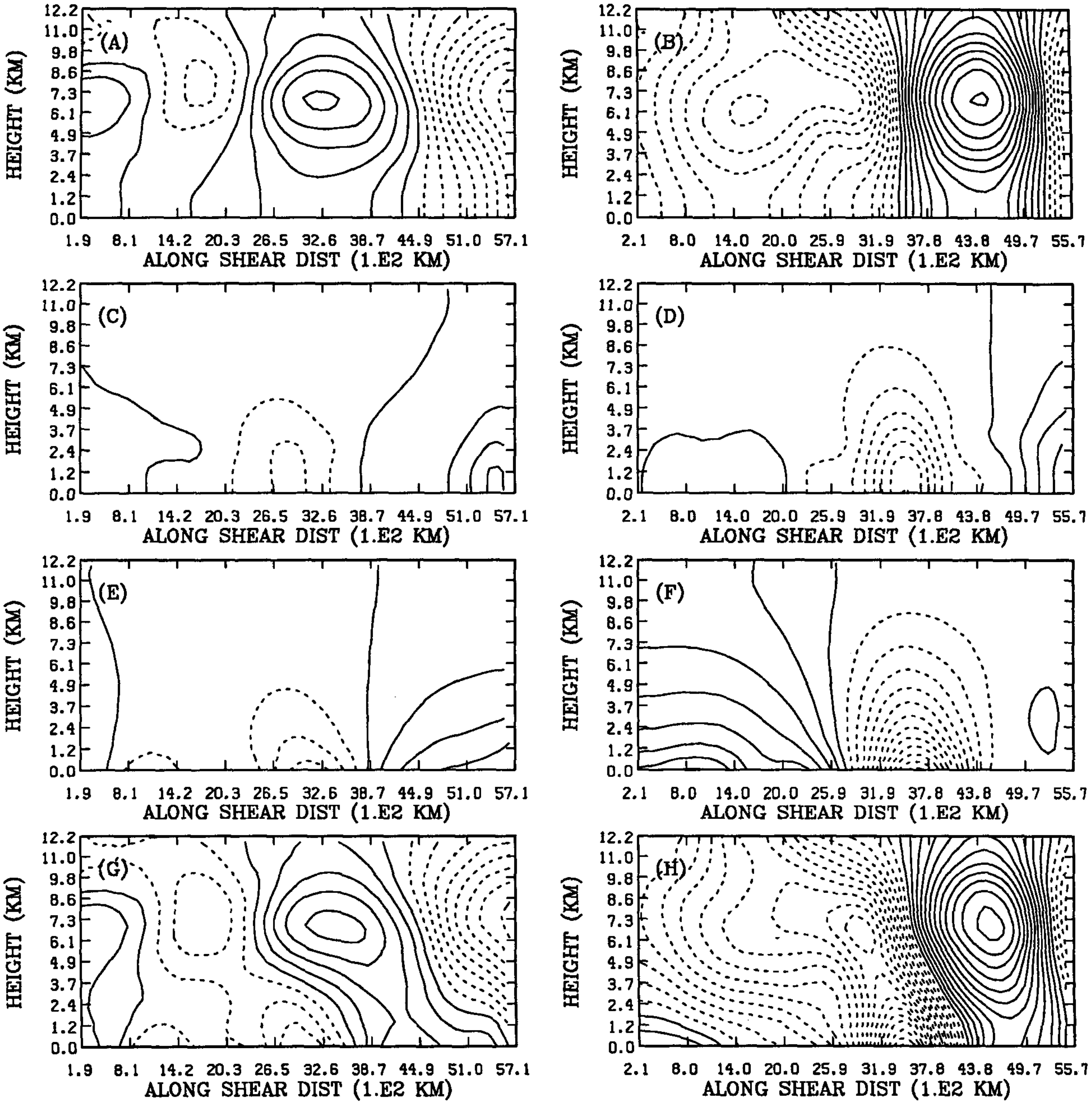

FIG. 14. Cross sections of perturbations geopotential height for 1200 UTC 4 February (left column) and 1200 UTC 5 February (right column). Contour interval is 2 dam, dashed lines for negative values. Cross sections are taken along the mean shear between 1000 and 400 mb, indicated by the heavy dashed lines in Figs. 4c and 4g; (a) and (b) show height perturbations related to the upper EPV (500 mb and up); (c) and (d) for lower EPV (850 mb and 700 mb); (e) and (f) for θ_B; (g) and (h) for the total perturbation. Mandatory levels from 1000 to 100 mb are plotted, the ordinate scale is linear in pseudoheight.

The techniques outlined in this paper may also be applied to diagnosing forecast errors in numerical weather prediction models. In addition, by phrasing predictability studies in terms of PV, one might better understand the nature of forecast sensitivity to errors in the initial conditions. Certain components of the PV distribution, especially the configuration of the dynamic tropopause, seem to warrant special attention. It is important that data and models have enough resolution to accurately depict this feature.

We hope the continued application of the quantitative diagnostics discussed in this paper will yield further insights into the dynamics of synoptic and large-scale systems. This promises to provide a common ground from which observational, numerical, and theoretical work may be easily compared. Work is currently in progress to examine more cyclogenesis cases, with different structures and intensities, in order to realize a more complete and fundamental conceptual picture of synoptic-scale dynamics.

Acknowledgments. This work represents a portion of the first author's Ph.D. dissertation at the Massachusetts Institute of Technology. The authors would like to thank Jerry Olsen of the National Center for Atmospheric Research, Boulder, Colorado, for assistance is obtaining the NMC data. In addition, the authors wish to thank Randy Dole and Peter Neilley of MIT for their comments. The original thesis work was supported by NSF Grant ATM 8513871.

APPENDIX A

Details of Inversion Technique

First we nondimensionalize relations (2.1) and (2.3) by defining

$$\Psi = \frac{S\Pi^2}{F}\tilde{\Psi},$$

$$\Phi = S\Pi^2\tilde{\Phi},$$

$$q = \frac{SFg\kappa C_p}{p_0}\left(\frac{p}{p_0}\right)^{\kappa-1}\tilde{q},$$

where S is a characteristic static stability $(-\partial\theta/\partial\pi)$, $F = 2\Omega$ $(\Omega = 7.29 \times 10^{-5}\ \mathrm{s}^{-1})$, Π is the characteristic vertical scale, and tildes denote nondimensional quantities. We also nondimensionalize the horizontal independent variables as $a^{-1}(\partial/\partial\lambda,\ \partial/\partial\phi) = L^{-1} \times (\partial/\partial\tilde{\lambda}, \partial/\partial\tilde{\phi})$ with L, the deformation radius, defined as $L^2 \equiv S\Pi^2/F^2$. Using these relations, (2.1) and (2.3) can be written as

$$\nabla^2\Phi = \sin\phi\nabla^2\Psi + \frac{L}{a}\cos\phi\frac{\partial\Psi}{\partial\phi} + \frac{2}{\cos^2\phi}\frac{\partial(\partial\Psi/\partial\lambda,\ \partial\Psi/\partial\phi)}{\partial(\lambda,\ \phi)} \quad \text{(A.1)}$$

$$q = (\sin\phi + \nabla^2\Psi)\frac{\partial^2\Phi}{\partial\pi^2} - \frac{1}{\cos^2\phi}\frac{\partial^2\Psi}{\partial\lambda\partial\pi}\frac{\partial^2\Phi}{\partial\lambda\partial\pi} - \frac{\partial^2\Psi}{\partial\phi\partial\pi}\frac{\partial^2\Phi}{\partial\phi\partial\pi} \quad \text{(A.2)}$$

where tildes have been omitted.

Our method consists of solving the sum of (A.1) and (A.2) for Ψ and using this solution to solve the difference of (A.1) and (A.2) for Φ:

$$\left[\sin\phi + \frac{\partial^2\Phi^{(\nu)}}{\partial\pi^2}\right]\nabla^2\Psi^{(\nu+1)} = q + \nabla^2\Phi^{(\nu)} - \sin\phi\frac{\partial^2\Phi^{(\nu)}}{\partial\pi^2} - N_2[\Psi^{(\nu)}, \Phi^{(\nu)}] - N_1[\Psi^{(\nu)}] \quad \text{(A.3)}$$

$$\nabla^2\Phi^{(\nu+1)} + [\sin\phi + \nabla^2\Psi^{(\nu+1)}]\frac{\partial^2\Phi^{(\nu+1)}}{\partial\pi^2} = q + \sin\phi\nabla^2\Psi^{(\nu+1)} - N_2[\Psi^{(\nu+1)}, \Phi^{(\nu)}] + N_1[\Psi^{(\nu+1)}]. \quad \text{(A.4)}$$

Here N_1 and N_2 represent the last two terms on the right-hand side of (A.1) and (A.2), respectively. If the static stability and absolute vorticity are positive, the (A.3) and (A.4) are elliptic equations for $\Psi^{(\nu+1)}$ and $\Phi^{(\nu+1)}$, respectively. Dividing (A.3) by $[\sin\phi + \partial^2\Phi^{(\nu)}/\partial\pi^2]$, results in a simple two-dimensional Poisson equation.

We proceed toward a solution of the system (A.1) and (A.2) by iterating on the system (A.3) and (A.4) until both (A.3) and (A.4) are satisfied by $\Phi^{(\nu+1)}$ and $\Psi^{(\nu+1)}$ to dimensional accuracies of 1 $\mathrm{m}^2\ \mathrm{s}^{-2}$ and 10^4 $\mathrm{m}^2\ \mathrm{s}^{-1}$, respectively. By "accuracy," we mean the largest change in the domain of either streamfunction or geopotential from one iteration to the next.

To solve the finite-difference forms of (A.3) and (A.4) individually, we use standard successive overrelaxation (SOR), although faster methods may be used. Each updated solution, $\Phi^{(\nu+1)}$ and $\Psi^{(\nu+1)}$, is underrelaxed by a factor between 0.6 and 0.8. While (A.3) and (A.4) converge individually, the system itself will not converge unless underrelaxation is performed. In addition, ellipticity of (A.1) and (A.2) is dependent on the PV being positive, and our solution method did not converge unless we imposed that condition on the observed PV field. Negative PV values were set to a small positive constant (10^{-2} PVU). For the grid we used, consisting of 45 points in the longitudinal direction, 26 latitude points, and 8 interior levels, convergence required about 6–8 min on a VAX 3500.

APPENDIX B

The Prognostic Balance Equations

We start by taking the local time derivative of (2.1) and (2.3) by which we obtain

$$\nabla^2\Phi_t = \nabla\cdot(f\nabla\Psi_t) + \frac{2}{a^4\cos^2\phi} \times \left[\frac{\partial(\partial\Phi_t/\partial\lambda,\ \partial\Psi/\partial\phi)}{\partial(\lambda,\ \phi)} + \frac{\partial(\partial\Phi/\partial\lambda,\ \partial\Psi_t/\partial\phi)}{\partial(\lambda,\ \phi)}\right] \quad \text{(B.1)}$$

$$\frac{\partial q}{\partial t} = \frac{g\kappa\pi}{p}\left[(f + \nabla^2\Psi)\frac{\partial^2\Phi_t}{\partial\pi^2} + \frac{\partial^2\Phi}{\partial\pi^2}\nabla^2\Psi_t - \frac{1}{a^2\cos^2\phi}\left(\frac{\partial^2\Psi}{\partial\lambda\partial\pi}\frac{\partial^2\Phi_t}{\partial\lambda\partial\pi} + \frac{\partial^2\Phi}{\partial\lambda\partial\pi}\frac{\partial^2\Psi_t}{\partial\lambda\partial\pi}\right) - \frac{1}{a^2}\left(\frac{\partial^2\Psi}{\partial\phi\partial\pi}\frac{\partial^2\Phi_t}{\partial\phi\partial\pi} + \frac{\partial^2\Phi}{\partial\phi\partial\pi}\frac{\partial^2\Psi_t}{\partial\phi\partial\pi}\right)\right], \quad \text{(B.2)}$$

where subscript t denotes $\partial/\partial t$. The EPV tendency can be expressed

$$\frac{\partial q}{\partial t} = -\mathbf{v}_h \cdot \nabla q - \omega^* \frac{\partial q}{\partial \pi} + \frac{g\kappa\pi}{p}\left[\boldsymbol{\eta} \cdot \nabla\left(\frac{d\theta}{dt}\right) + \nabla\theta \cdot \nabla \times \mathbf{F}\right] \quad \text{(B.3)}$$

where $\omega^* \equiv d\pi/dt$, $\mathbf{v}_h = \mathbf{v}_\psi + \mathbf{v}_\chi$ and $\mathbf{F}$ is the frictional force. The only nonconservative term we will deal with explicitly is latent heat release.

The presence of the vertical velocity and irrotational winds [which are formally retained in the prognostic equations, Krishnamurti (1968), Iversen and Nordeng (1984)] means that we cannot simply advect EPV with the nondivergent wind, analogous to geostrophic advection of PPV in QG theory. The vertical and irrotational flows are obtained in a self-consistent, iterative technique whereby EPV is advected by the nondivergent wind, the resulting flow tendencies inverted, vertical velocity and divergence deduced, and the EPV advection estimate improved. To solve for the vertical velocity, we invert an ω equation similar to that in Iversen and Nordeng, obtained as ∇^2 (thermodynamic equation) $-(f\partial/\partial\pi)$ (balanced vorticity equation) $-\partial/\partial\pi)$ (B.1) (Gent and McWilliams 1983). The relation is

$$\begin{aligned} &f\eta \frac{\partial}{\partial \pi}\left[\pi^{1-1/\kappa} \frac{\partial}{\partial \pi}(\pi^{1/\kappa-1}\omega^*)\right] + \nabla^2\left(\frac{\partial^2 \Phi}{\partial \pi^2}\omega^*\right) \\ &\quad - \frac{f}{a^2}\frac{\partial}{\partial \pi}\left(\frac{\partial^2 \Psi}{\partial \phi \partial \pi}\frac{\partial \omega^*}{\partial \pi} + \frac{1}{\cos^2\phi}\frac{\partial^2 \Psi}{\partial \lambda \partial \pi}\frac{\partial \omega^*}{\partial \lambda}\right) \\ &\quad + \left(f\frac{\partial \eta}{\partial \pi}\frac{1/\kappa - 1}{\pi} - f\frac{\partial^2 \eta}{\partial \pi^2}\right)\omega^* = \nabla^2(\mathbf{v}_h \cdot \nabla\theta) \\ &\quad + f\frac{\partial}{\partial \pi}(\mathbf{v}_h \cdot \nabla \eta) - \nabla f \cdot \nabla\left(\frac{\partial^2 \Psi}{\partial \pi \partial t}\right) \\ &\quad - \frac{\partial}{\partial \pi}(J) + \nabla^2\left(\frac{d\theta}{dt}\right), \quad \text{(B.4)} \end{aligned}$$

where J stands for the Jacobian terms in (B.1) and friction has been neglected. The first two terms on each side of (B.4) have direct counterparts in the QG omega equation. Coupling between (B.4) and (B.1), (B.2) and (B.3) results from the Jacobian terms, diabatic heating, and vertical advection of EPV. Relation (B.4), combined with mass continuity

$$\nabla^2\chi + \pi^{1-1/\kappa}\frac{\partial}{\partial \pi}(\pi^{1/\kappa-1}\omega^*) = 0 \quad \text{(B.5)}$$

completes the system of five equations for the unknowns ($\partial\Psi/\partial t$, $\partial\Phi/\partial t$, $\partial q/\partial t$, ω^* and χ).

We incorporate the effects of latent heat release only from nonconvective clouds where the air is ascending on a broad scale. Because the latent heating is proportional to ω^*, its effect is equivalent to a locally reduced effective static stability. To satisfy ellipticity, the effective stability must be positive. We enforce this by requiring positive saturation EPV (section 4) and adjust the effective stability until this is so. Because moisture analyses seldom indicate true saturation in areas of precipitation, we define saturation with a threshold relative humidity of 80%. Results are not sensitive to threshold values between about 70% and 90%.

The system (B.1)–(B.5) is solved a by simultaneous relaxation method, which is straightforward to implement because the operators in (B.1), (B.2), (B.4), and (B.5) are linear. At each iteration step, we solve an algebraic system of equations [analogous to (A.11) and (A.12)] for the incremental changes in the tendencies, vertical motion, and divergence necessary to temporarily reduce errors in the previous guesses to zero. During the iteration process, the areas of ascent and reduced static stability are determined after each pass through the grid. The potential temperature tendency, evaluated from the full thermodynamic equation, sets the vertical derivative of $\partial\Psi/\partial t$ and $\partial\Phi/\partial t$ at the lower and upper boundaries (925 and 125 mb, respectively). Homogeneous lateral boundary conditions are applied for each field (see Gent and McWilliams 1983, for more appropriate conditions). We stagger the ω^* levels with respect to the mandatory levels, applying a topographic lower boundary condition at 1000 mb and $\omega^* = 0$ at 75 mb. Therefore, the vertical advection of potential temperature at 925 and 125 mb is nonzero, and the potential temperature tendency must be found by iteration. This, and the iteration for areas of reduced static stability, pose no convergence problems. The iteration cycle is stopped when the changes in the streamfunction tendency (scaled by f_0/g) and height tendency are both less than 0.1 m per 12 h.

REFERENCES

Bretherton, F. P., 1966: Critical layer instability in baroclinic flows. *Quart. J. Roy. Meteor. Soc.*, **92,** 325–334.

Charney, J. G., 1947: The dynamics of long waves in a baroclinic westerly current. *J. Meteor.*, **4,** 135–163.

——, 1955: The use of primitive equations of motion in numerical prediction. *Tellus,* **7,** 22–26.

——, 1962 Integration of the primitive and balance equations. *Proc. Symp. Numerical Weather Prediction, Tokyo,* 131–152.

——, and M. E. Stern, 1962: On the stability of internal baroclinic jets in a rotating atmosphere. *J. Atmos. Sci.*, **19,** 159–172.

Danard, M. B., 1964: On the influence of released latent heat on cyclone development. *J. Appl. Meteor.*, **3,** 27–37.

Danielsen, E. F., 1968: Stratospheric-tropospheric exchange based on radioactivity, ozone, and potential vorticity. *J. Atmos. Sci.*, **25,** 502–518.

Davis, C. A., 1990: Cyclogenesis diagnosed with potential vorticity. Ph.D. thesis. Massachusetts Institute of Technology. 194 pp. [Available from author at National Center for Atmospheric Research, P.O. Box 3000, Boulder CO. 80307.]

Eady, T. E., 1949: Long waves and cyclone waves. *Tellus,* **1,** 33–52.

Edmon, H. J., Jr., B. J. Hoskins and M. E. McIntyre, 1980: Eliassen–Palm cross sections for the troposphere. *J. Atmos. Sci.*, **37,** 2600–2616.

Eliassen, A., and E. Kleinschmidt, 1957: Dynamic meteorology. *Handbuch der Physik,* Vol 48, Springer Verlag, 1–154.

Emanuel, K. A., 1988: Observational evidence of slantwise convective adjustment. *Mon. Wea. Rev.*, **116,** 1805–1815.

——, M. Fantini and A. J. Thorpe, 1987: Baroclinic instability in an environment of small stability to slantwise moist convection. Part I: Two-dimensional models. *J. Atmos. Sci.*, **44,** 1559–1573.

Ertel H., 1942: Ein neuer hydrodynamischer wirbelsatz. *Meteor. Z.*, **59,** 271–281.

Farrell, B. F., 1984: Modal and nonmodal baroclinic waves. *J. Atmos. Sci.*, **41,** 668–673.

——, 1989: On the optimal excitation of baroclinic waves. *J. Atmos. Sci.*, **46,** 1193–1206.

Gent, P. R., and J. G. McWilliams, 1983: Consistent balanced models in bounded and periodic domains. *Dyn. Atmos. Oceans,* **7,** 67–93.

Gyakum, J. R., 1983: On the evolution of the *QE II* storm. II: Dynamic and thermodynamic structure. *Mon. Wea. Rev.*, **111,** 1156–1173.

Haltiner, G. J., and R. T. Williams, 1980: *Numerical Prediction and Dynamic Meteorology.* 2d ed. Wiley and Sons, 477 pp.

Hoskins, B. J., and F. P. Bretherton, 1972: Atmospheric frontogenesis models: Mathematical formulation and solution. *J. Atmos. Sci.*, **29,** 11–37.

——, M. E. McIntyre and A. W. Robertson, 1985: On the use and significance of isentropic potential vorticity maps. *Quart. J. Roy. Meteor. Soc.*, **111,** 877–946.

——, and P. Berrisford, 1988: A potential vorticity perspective of the storm of 15–16 October 1987. *Weather,* **43,** 122–129.

Iversen, T., and T. E. Nordeng, 1984: A hierarchy of nonlinear filtered models—numerical solutions. *Mon. Wea. Rev.*, **112,** 2048–2059.

Krishnamurti, T. N., 1968: A diagnostic balanced model for studies of weather systems of low and high latitudes, Rossby number less than 1. *Mon. Wea. Rev.*, **96,** 197–207.

Kuo, Y. H., and R. J. Reed, 1988: Numerical simulation of an explosively deepening cyclone in the eastern Pacific. *Mon. Wea. Rev.*, **116,** 2081–2105.

——, R. J. Reed and S. Low-Nam, 1990a: Effects of surface energy fluxes during the early development and rapid intensification stages of seven explosive cyclones in the western Atlantic. *Mon. Wea. Rev.*, **119,** 457–476.

——, M. A. Shapiro and E. G. Donall, 1990b: The interaction between baroclinic and diabatic processes in a numerical simulation of a rapidly intensifying extratropical marine cyclone. *Mon. Wea. Rev.*, **119,** 368–384.

Manabe, S., 1956: On the contribution of heat released by condensation to the change in pressure pattern. *J. Meteorol. Soc. Jpn.*, **34,** 12–24.

Montgomery, M. T., and B. F. Farrell, 1991: Moist surface frontogenesis associated with interior potential vorticity anomalies in a semigeostrophic model. *J. Atmos. Sci.*, **48,** 343–367.

Pedlosky, J., 1979: *Geophysical Fluid Dynamics.* Springer Verlag.

Petterssen, S., and S. J. Smebye, 1971: On the development of extratropical cyclones. *Quart. J. Roy. Meteorol. Soc.*, **97,** 457–482.

——, G. E. Dunn and L. L. Means, 1955: Report on an experiment in forecasting of cyclone development. *J. Appl. Meteor.*, **12,** 58–67.

Robinson, W. A., 1988: Analysis of LIMS data by potential vorticity inversion. *J. Atmos. Sci.*, **45,** 2319–2342.

——, 1989: On the structure of potential vorticity in baroclinic instability. *Tellus,* **41,** 275–284.

Rossby, C. G., 1940: Planetary flow patterns in the atmosphere. *Quart. J. Roy. Meteor. Soc.*, **66,**(Suppl) 68–87.

Sanders, F., 1986: Explosive cyclogenesis over the west central North Atlantic Ocean 1981–1984. Part I: Composite structure and mean behavior. *Mon. Wea. Rev.*, **114,** 1781–1794.

——, 1988: Life history of mobile troughs in the upper westerlies. *Mon. Wea. Rev.*, **118,** 2629–2648.

——, and L. F. Bosart, 1985: Mesoscale structure in the Megalopolitan snowstorm of 11–12 February 1983. Part I: Frontogenetical forcing and symmetric instability. *J. Atmos. Sci.*, **42,** 1050–1061.

Simmons, A. J., and B. J. Hoskins, 1978: The life cycles of some nonlinear baroclinic waves. *J. Atmos. Sci.*, **35,** 414–432.

Thorpe, A. J., 1986: Synoptic scale disturbances with circular symmetry. *Mon. Wea. Rev.*, **114,** 1384–1389.

Tracton, M. S., 1973: The role of cumulus convection in the development of extratropical cyclones. *Mon. Wea. Rev.*, **101,** 573–592.

Trenberth, K. E., and J. G. Olson, 1988: Evaluation of NMC global analysis: 1979–1987. NCAR Tech. Note TN-299+STR. [Available from National Center for Atmospheric Research, Boulder, CO. 80307-3000.]

Uccellini, L. W., R. A. Petersen, K. F. Brill, P. J. Kocin and H. J. Tuccillo, 1987: Synergistic interactions between an upper-level jet streak and diabatic processes that influence the development of a low-level jet and a secondary coastal cyclone. *Mon. Wea. Rev.*, **115,** 2227–2261.

Whitaker, J. S., L. W. Uccellini and K. F. Brill, 1988: A model-based diagnostic study of the rapid development phase of the Presidents' Day cyclone. *Mon. Wea. Rev.*, **116,** 2337–2365.